Electromagnetic structure of $A = 2$ and 3 nuclei in chiral effective field theory

M. Piarulli,[1] L. Girlanda,[2] L. E. Marcucci,[3,4] S. Pastore,[5] R. Schiavilla,[1,6] and M. Viviani[4]
[1]*Department of Physics, Old Dominion University, Norfolk, Virginia 23529, USA*
[2]*Department of Mathematics and Physics, University of Salento, and INFN-Lecce, I-73100 Lecce, Italy*
[3]*Department of Physics, University of Pisa, I-56127 Pisa, Italy*
[4]*INFN-Pisa, I-56127 Pisa, Italy*
[5]*Physics Division, Argonne National Laboratory, Argonne, Illinois 60439, USA*
[6]*Jefferson Lab, Newport News, Virginia 23606, USA*
(Received 5 December 2012; published 30 January 2013)

Background: The $A = 2$ and 3 form factors are among the observables of choice for testing models of nuclear interactions and associated electromagnetic charge and current operators. Here we investigate the validity of the chiral-effective-field-theory (χEFT) approach to describe the strong-interaction dynamics in these few-nucleon systems and their response to electromagnetic probes.
Purpose: The objectives of the present work are twofold. The first is to address and resolve some of the differences present in independent, χEFT derivations up to one loop, recently appearing in the literature, of the nuclear charge and current operators. The second objective is to provide a complete set of χEFT and hybrid predictions for the structure functions and tensor polarization of the deuteron, for the charge and magnetic form factors of ^{3}He and ^{3}H, and for the charge and magnetic radii of these few-nucleon systems.
Methods: The calculations use wave functions derived from either chiral or conventional two- and three-nucleon potentials and Monte Carlo methods to evaluate the relevant matrix elements.
Results: In reference to the two objectives mentioned earlier, we find that (i) there are no differences between the χEFT magnetic dipole operator at one loop derived in our formalism and that obtained by Kölling *et al.* [Phys. Rev. C **80**, 045502 (2009)] with the unitary transformation method and (ii) there is excellent agreement between theory and experiment for the static properties and elastic form factors of these $A = 2$ and 3 nuclei up to momentum transfers $q \lesssim 2.0$–2.5 fm^{-1}. A complete analysis of the results is provided.
Conclusions: Nuclear χEFT provides a very satisfactory description of the isoscalar and isovector charge and magnetic structure of the $A = 2$ and 3 nuclei at low momentum transfers $q \lesssim 3m_\pi$. In particular, contributions from two-body charge and current operators are crucial for bringing theory into close agreement with experiment. At higher q values the present χEFT predictions are similar to those obtained in the hybrid approach, as well as in older studies based on the conventional meson-exchange picture, and fail to reproduce the measured $A = 2$ and 3 form factors in the diffraction region.

DOI: 10.1103/PhysRevC.87.014006 PACS number(s): 12.39.Fe, 13.40.−f, 21.45.−v, 27.10.+h

I. INTRODUCTION

Over the past two decades, chiral effective field theory (χEFT), originally proposed by Weinberg in a series of papers in the early 1990s [1], has blossomed into a very active field of research. The chiral symmetry exhibited by quantum chromodynamics (QCD) severely restricts the form of the interactions of pions among themselves and with other particles. In particular, the pion couples to baryons, such as nucleons and Δ isobars, by powers of its momentum Q, and the Lagrangian describing these interactions can be expanded in powers of Q/Λ_χ, where $\Lambda_\chi \sim 1$ GeV specifies the chiral-symmetry-breaking scale. As a result, classes of Lagrangians emerge, each characterized by a given power of Q/Λ_χ and each involving a certain number of unknown coefficients, so-called low-energy constants (LECs), which are then determined by fits to experimental data (see, for example, the review papers [2,3] and references therein). Thus, χEFT provides, on the one hand, a direct connection between QCD and its symmetries, in particular chiral symmetry, and the strong and electroweak interactions in nuclei and, on the other hand, a practical calculational scheme susceptible, in principle, to systematic improvement. In this sense, it can be justifiably argued to have put low-energy few-nucleon physics on a more fundamental basis.

Nuclear electromagnetic charge and current operators in χEFT up to one loop were derived originally by Park *et al.* [4] in covariant perturbation theory. Recently, two independent derivations, based on time-ordered perturbation theory (TOPT), have appeared in the literature, one by some of the present authors [5,6] and the other by Kölling *et al.* [7,8]. The expressions in Refs. [5–7] for the two-pion-exchange charge and current operators are in agreement with each other. Differences between the expressions reported in Refs. [5,6] and those in Ref. [8] are found in some of the loop corrections to the one-pion-exchange (OPE) and short-range currents as well as the minimal currents originating from four-nucleon contact interactions involving two gradients of the nucleon fields. The differences in the loop corrections have their origin in the different implementations of TOPT adopted in Refs. [5,6,8] and relate to the treatment of reducible diagrams. One of the objectives of the present work is to resolve some of these differences. This is addressed in Sec. II and Appendices A and B.

The other objective is to provide predictions for the charge and magnetic radii and form factors of the deuteron and trinucleons (^{3}He and ^{3}H), by utilizing two- and three-nucleon potentials derived either in χEFT or in the conventional framework, in combination with the charge and current

 ©2013 American Physical Society

operators obtained here. The methods used to carry out the calculations are discussed in Sec. III, and a detailed analysis of the results is presented in Sec. IV. This last section is organized into three subsections: the first illustrates the different strategies adopted for the determination of the low-energy constants that characterize the current operator up to one loop (i.e., no unknown LECs enter the one-loop charge operator); the second and third report results, respectively, for the $A(q)$ and $B(q)$ structure functions and tensor polarization $T_{20}(q)$ of the deuteron and for the charge and magnetic form factors of ^{3}He and ^{3}H, as well as results for the charge and magnetic radii of these few-nucleon systems. The conclusions are summarized in Sec. V, while details of the evaluation of the loop integrals entering the charge operator are relegated in Appendix C.

There have been earlier χEFT studies of the deuteron electromagnetic structure in Refs. [9–11] and, most recently, in Ref. [12]—this latter work has focused on the $B(q)$ structure function. To the best of our knowledge, however, one-loop χEFT predictions for the ^{3}He and ^{3}H elastic form factors have not been reported.

In reference to the two objectives mentioned earlier, we find that (i) there are no differences between the χEFT magnetic dipole operator at one loop derived in our formalism and that obtained by Kölling *et al.* [8] with the unitary transformation method and (ii) there is excellent agreement between theory and experiment for the static properties and elastic form factors of these $A = 2$ and 3 nuclei up to momentum transfers $q \lesssim 2.0$–2.5 fm^{-1}. In particular, contributions from two-body charge and current operators are crucial for bringing theory into this close agreement with experiment. At higher q values the present χEFT predictions are similar to those obtained in the hybrid approach, as well as in older studies based on the conventional meson-exchange picture, and they fail to reproduce the measured $A = 2$ and 3 form factors in the diffraction region.

II. NUCLEAR CHARGE AND CURRENT OPERATORS UP TO ONE LOOP

The two-nucleon current ($\mathbf{j}$) and charge (ρ) operators have been derived in χEFT up to one loop (to order eQ) in Refs. [5,6], respectively. In the following, we denote the momentum due to the external electromagnetic field with $\mathbf{q}$, and we define

$$\mathbf{k}_i = \mathbf{p}_i' - \mathbf{p}_i, \quad \mathbf{K}_i = (\mathbf{p}_i' + \mathbf{p}_i)/2, \tag{2.1}$$

$$\mathbf{k} = (\mathbf{k}_1 - \mathbf{k}_2)/2, \quad \mathbf{K} = \mathbf{K}_1 + \mathbf{K}_2, \tag{2.2}$$

where $\mathbf{p}_i$ ($\mathbf{p}_i'$) is the initial (final) momentum of nucleon i. We further define

$$\mathbf{j} = \sum_{n=-2}^{+1} \mathbf{j}^{(n)}, \quad \rho = \sum_{n=-3}^{+1} \rho^{(n)}, \tag{2.3}$$

where the superscript n in $\mathbf{j}^{(n)}$ and $\rho^{(n)}$ specifies the order eQ^n in the power counting. The lowest-order (LO) contributions $\mathbf{j}^{(-2)}$ and $\rho^{(-3)}$ consist of the single-nucleon current and charge operators, respectively:

$$\mathbf{j}^{(-2)} = \frac{e}{2m_N}[2\,e_{N,1}(q^2)\,\mathbf{K}_1 + i\,\mu_{N,1}(q^2)\,\boldsymbol{\sigma}_1 \times \mathbf{q}] \times \delta(\mathbf{p}_2' - \mathbf{p}_2) + 1 \rightleftharpoons 2 \tag{2.4}$$

and

$$\rho^{(-3)} = e\,e_{N,1}(q^2)\,\delta(\mathbf{p}_2' - \mathbf{p}_2) + 1 \rightleftharpoons 2, \tag{2.5}$$

where m_N is the nucleon mass, $\mathbf{q} = \mathbf{k}_i$ with $i = 1$ or 2 (where the δ functions enforcing overall momentum conservation $\mathbf{q} = \mathbf{k}_1$ have been dropped for simplicity here and in the following),

$$e_{N,i}(q^2) = \frac{G_E^S(q^2) + G_E^V(q^2)\,\tau_{i,z}}{2}, \qquad \mu_{N,i}(q^2) = \frac{G_M^S(q^2) + G_M^V(q^2)\,\tau_{i,z}}{2}, \tag{2.6}$$

and G_E^S (G_E^V) and G_M^S (G_M^V) denote the isoscalar (isovector) combinations of the proton and neutron electric (E) and magnetic (M) form factors, normalized as $G_E^S(0) = G_E^V(0) = 1$, $G_M^S(0) = 0.880\mu_N$, and $G_M^V(0) = 4.706\mu_N$ in units of the nuclear magneton μ_N. The counting eQ^{-2} (eQ^{-3}) of the leading-order current (charge) operator results from the product of a factor eQ (eQ^0) due to the coupling of the external electromagnetic field to the individual nucleons and the factor Q^{-3} from the momentum δ function entering this type of disconnected contributions. Of course, this counting ignores the fact that the nucleon form factors themselves also have a power-series expansion in Q. Here, they are taken from fits to elastic electron scattering data off the proton and deuteron [13]—specifically, the Höhler parametrization [14]—rather than derived consistently in chiral perturbation theory (χPT) [15]. The calculations of the $A = 2$ and 3 nuclei elastic form factors that follow are carried out in the Breit frame, in which the electron-energy transfer vanishes. Hence, the hadronic electromagnetic form factors are evaluated at four-momentum transfer $q^\mu q_\mu = -q^2$.

At order $n = -1$ (NLO) there is a one-pion-exchange (OPE) contribution to the current operator which reads

$$\mathbf{j}^{(-1)} = -i\,e\frac{g_A^2}{F_\pi^2}\,G_E^V(q^2)\,(\boldsymbol{\tau}_1 \times \boldsymbol{\tau}_2)_z\left(\boldsymbol{\sigma}_1 - \mathbf{k}_1\frac{\boldsymbol{\sigma}_1\cdot\mathbf{k}_1}{\omega_{k_1}^2}\right) \times \frac{\boldsymbol{\sigma}_2\cdot\mathbf{k}_2}{\omega_{k_2}^2} + 1 \rightleftharpoons 2, \tag{2.7}$$

where we have defined $\omega_k^2 = k^2 + m_\pi^2$, with m_π being the pion mass. However, there are no $n = -2$ contributions to the charge operator. The presence of the isovector electric form factor G_E^V in $\mathbf{j}^{(-1)}$ follows from the continuity equation

$$\mathbf{q}\cdot\mathbf{j}^{(-1)} = \left[v_\pi^{(0)}, \rho^{(-3)}\right], \tag{2.8}$$

where $[\cdots,\cdots]$ denotes the commutator, $\rho^{(-3)}$ is the charge operator given in Eq. (2.5), and $v_\pi^{(0)}$ is the static OPE potential

$$v_\pi^{(0)}(\mathbf{k}) = -\frac{g_A^2}{F_\pi^2}\,\boldsymbol{\tau}_1\cdot\boldsymbol{\tau}_2\,\frac{\boldsymbol{\sigma}_1\cdot\mathbf{k}\,\boldsymbol{\sigma}_2\cdot\mathbf{k}}{\omega_k^2}. \tag{2.9}$$

The left-hand side of Eq. (2.8) is of order Q^0, the same as the right-hand side since the commutator brings in an additional factor Q^3 due to the implicit momentum integrations. It should be emphasized that the continuity equation requires that the

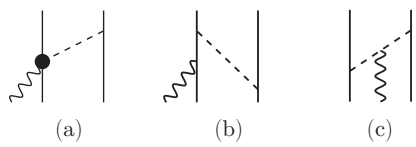

FIG. 1. Diagrams illustrating the two-body charge operators at order $n = 0$ or eQ^0. Nucleons, pions, and photons are denoted by solid, dashed, and wavy lines, respectively. The solid circle in panel (a) is associated with a $\gamma\pi N$ vertex of order eQ. Only one among the possible time orderings is shown.

same form factor be used to describe the electromagnetic structure of the hadrons in the longitudinal part of the current operator and in the charge operator. However, it places no restrictions on the electromagnetic form factors which may be used in the transverse parts of the current. By ignoring this ambiguity, the choice made here (G_E^V) satisfies the "minimal" requirement of current conservation [16].

Relativistic corrections to the leading-order one-body current and charge operators enter, respectively, at $n = 0$ and $n = -1$ (both denoted as N2LO) and are given by

$$\begin{aligned}\mathbf{j}^{(0)} = &-\frac{e}{8\,m_N^3} e_{N,1}(q^2)\big[2\big(K_1^2 + q^2/4\big)(2\,\mathbf{K}_1 + i\,\boldsymbol{\sigma}_1 \times \mathbf{q}) \\ &+ \mathbf{K}_1 \cdot \mathbf{q}\,(\mathbf{q} + 2\,i\,\boldsymbol{\sigma}_1 \times \mathbf{K}_1)\big] \\ &- \frac{i\,e}{8\,m_N^3}[\,\mu_{N,1}(q^2) - e_{N,1}(q^2)] \\ &\times [\mathbf{K}_1 \cdot \mathbf{q}\,(4\,\boldsymbol{\sigma}_1 \times \mathbf{K}_1 - i\,\mathbf{q}) - (2\,i\,\mathbf{K}_1 - \boldsymbol{\sigma}_1 \times \mathbf{q})\,q^2/2 \\ &+ 2\,(\mathbf{K}_1 \times \mathbf{q})\,\boldsymbol{\sigma}_1 \cdot \mathbf{K}_1]\,\delta(\mathbf{p}_2' - \mathbf{p}_2) + 1 \rightleftharpoons 2, \qquad (2.10)\end{aligned}$$

$$\begin{aligned}\rho^{(-1)} = &-\frac{e}{8\,m_N^2}\,[\,2\,\mu_{N,1}(q^2) - e_{N,1}(q^2)] \\ &\times (q^2 + 2\,i\,\mathbf{q} \cdot \boldsymbol{\sigma}_1 \times \mathbf{K}_1)\,\delta(\mathbf{p}_2' - \mathbf{p}_2) + 1 \rightleftharpoons 2, \qquad (2.11)\end{aligned}$$

while the $n = 0$ (N3LO) OPE two-body charge operators, illustrated in Fig. 1, read

$$\begin{aligned}\rho_{\rm a}^{(0)} = &\frac{e}{2\,m_N}\frac{g_A^2}{F_\pi^2}\big[G_E^S(q^2)\,\boldsymbol{\tau}_1 \cdot \boldsymbol{\tau}_2 + G_E^V(q^2)\,\tau_{2z}\big] \\ &\times \frac{\boldsymbol{\sigma}_1 \cdot \mathbf{q}\;\boldsymbol{\sigma}_2 \cdot \mathbf{k}_2}{\omega_{k_2}^2} + 1 \rightleftharpoons 2, \qquad (2.12)\end{aligned}$$

$$\begin{aligned}\rho_{\rm b}^{(0)}(\nu) = &-\frac{e}{4\,m_N}\frac{g_A^2}{F_\pi^2}\frac{\boldsymbol{\sigma}_1 \cdot \mathbf{k}_2\;\boldsymbol{\sigma}_2 \cdot \mathbf{k}_2}{\omega_{k_2}^4} \\ &\times \big[(1-\nu)\big[G_E^S(q^2)\,\boldsymbol{\tau}_1 \cdot \boldsymbol{\tau}_2 + G_E^V(q^2)\,\tau_{2,z}\big]\,\mathbf{q} \cdot \mathbf{k}_2 \\ &+ 2\,i\,G_E^V(q^2)\,(\boldsymbol{\tau}_1 \times \boldsymbol{\tau}_2)_z\,\mathbf{k}_2 \cdot [\,(1-\nu)\,\mathbf{K}_1 \\ &+ (1+\nu)\,\mathbf{K}_2]\big] + 1 \rightleftharpoons 2, \qquad (2.13)\end{aligned}$$

$$\begin{aligned}\rho_{\rm c}^{(0)} = &\,i\,\frac{e}{m_N}\,\frac{g_A^2}{F_\pi^2}\,G_\pi(q^2)\,(\boldsymbol{\tau}_1 \times \boldsymbol{\tau}_2)_z\;\mathbf{k}_1 \cdot \mathbf{K}_1\,\frac{\boldsymbol{\sigma}_1 \cdot \mathbf{k}_1\,\boldsymbol{\sigma}_2 \cdot \mathbf{k}_2}{\omega_{k_1}^2\,\omega_{k_2}^2} \\ &+ 1 \rightleftharpoons 2. \qquad (2.14)\end{aligned}$$

The operator of panel (a) of Fig. 1 is due to a $\gamma\pi N$ vertex of order eQ originating from the interaction Hamiltonian

$$\frac{e\,g_A}{2\,m_N F_\pi}\int d\mathbf{x}\,N^\dagger\,\boldsymbol{\sigma} \cdot (\boldsymbol{\nabla} A^0)(\boldsymbol{\tau} \cdot \boldsymbol{\pi} + \pi_z)N,$$

derived first by Phillips [10]. In the context of meson-exchange phenomenology, an operator of precisely this form results from considering the low-energy limit of the relativistic Born diagrams associated with virtual pion photoproduction amplitudes (see the review paper [17] and references therein). From this perspective, it appears reasonable to include the nucleon form factors G_E^S and G_E^V in Eq. (2.12).

The operator of panel (b) of Fig. 1 depends on the off-energy-shell extrapolation, specified by the parameter ν, adopted for the nonstatic corrections of order Q^2 to the OPE potential [18],

$$v_\pi^{(2)}(\mathbf{k}, \mathbf{K}; \nu) = (1 - 2\,\nu)\,\frac{v_\pi^{(0)}(\mathbf{k})}{\omega_k^2}\,\frac{(\mathbf{k} \cdot \mathbf{K})^2}{4\,m_N^2}. \qquad (2.15)$$

As shown in Ref. [18] (and within the present approach in Ref. [6]), different off-shell prescriptions for $v^{(2)}(\nu)$ and $\rho^{(0)}(\nu)$ are unitarily equivalent:

$$\begin{aligned}\rho^{(-3)} + \rho_{\rm b}^{(0)}(\nu) &= {\rm e}^{-i\,U(\nu)}\big[\rho^{(-3)} + \rho_{\rm b}^{(0)}(0)\big]\,{\rm e}^{+i\,U(\nu)} \\ &\simeq \rho^{(-3)} + \rho_{\rm b}^{(0)}(0) + [\rho^{(-3)}, i\,U^{(0)}(\nu)], \qquad (2.16)\end{aligned}$$

where the Hermitian operator $U(\nu)$ admits the expansion

$$U(\nu) = U^{(0)}(\nu) + U^{(1)}(\nu) + \cdots, \qquad (2.17)$$

and $U^{(0)}(\nu)$ and $U^{(1)}(\nu)$ (see below) have been constructed, respectively, in Refs. [18] and [6] [and, in this last paper, Eqs. (28) and (55), which give equivalent momentum-space expressions for $U^{(1)}(\nu)$, contain a typographical error: the imaginary unit on the left-hand side should be removed]. Phenomenological potentials, such as the Argonne v_{18} (AV18) [19], and χEFT potentials, such as those recently derived by Entem and Machleidt [20], make the choice $\nu = 1/2$ in Eq. (2.15); i.e., nonstatic corrections to the OPE potential are ignored.

The operator of panel (c), containing the $\gamma\pi\pi$ vertex, is obtained by expanding the energy denominators as [6]

$$\frac{1}{E_i - E_I - \omega_\pi} = -\frac{1}{\omega_\pi}\left[1 + \frac{E_i - E_I}{\omega_\pi} + \cdots\right], \qquad (2.18)$$

where E_I denotes NN (or $NN\gamma$) intermediate energies and ω_π the pion energy (or energies, as the case may be), and by noting that the leading (static) corrections vanish, when summed over the possible six time orderings. However, the terms proportional to the ratio $(E_i - E_I)/\omega_\pi$, which is of order Q, lead to the nonstatic operator given in Eq. (2.14). It is multiplied by the pion form factor $G_\pi(q^2)$, which we parametrize in vector-meson dominance and consistently with experimental data at low momentum transfers as

$$G_\pi(q^2) = \frac{1}{1 + q^2/m_\rho^2}, \qquad (2.19)$$

where m_ρ is the ρ-meson mass.

A. Current operators at order $n = 1$ (eQ)

The currents at order eQ (N3LO) are illustrated diagrammatically in Fig. 2, and they consist of (i) terms generated by minimal substitution in the four-nucleon contact interactions involving two gradients of the nucleon fields as well as by nonminimal couplings to the electromagnetic field, (ii) OPE

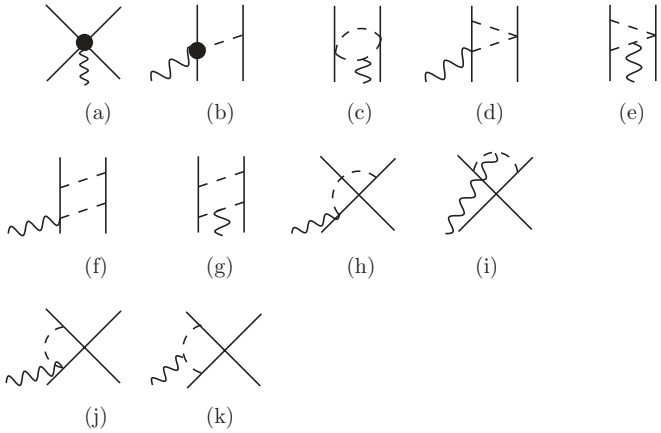

FIG. 2. Diagrams illustrating the two-body current operators at order $n = 1$ or eQ. Nucleons, pions, and photons are denoted by solid, dashed, and wavy lines, respectively. The solid circle in panel (b) is associated with a $\gamma\pi N$ vertex of order eQ^2. Only one among the possible time orderings is shown.

terms induced by $\gamma\pi N$ interactions beyond leading order, and (iii) one-loop two-pion-exchange (TPE) terms. We discuss them below.

The contact minimal and nonminimal currents, denoted by the subscripts "min" and "nm," respectively, are written as

$$\begin{aligned}\mathbf{j}^{(1)}_{\rm a,min} &= \frac{i\,e}{16}\,G^V_E(q^2)\,(\boldsymbol{\tau}_1\times\boldsymbol{\tau}_2)_z\,[(C_2+3\,C_4+C_7)\,\mathbf{k}_1\\ &\quad+(C_2-C_4-C_7)\,\mathbf{k}_1\;\boldsymbol{\sigma}_1\cdot\boldsymbol{\sigma}_2\\ &\quad+C_7\,\boldsymbol{\sigma}_1\cdot(\mathbf{k}_1-\mathbf{k}_2)\;\boldsymbol{\sigma}_2]-\frac{i\,e}{4}\,e_{N,1}(q^2)\,C_5\\ &\quad\times(\boldsymbol{\sigma}_1+\boldsymbol{\sigma}_2)\times\mathbf{k}_1+1\rightleftharpoons 2, \qquad (2.20)\\ \mathbf{j}^{(1)}_{\rm a,nm} &= -i\,e\big[G^S_E(q^2)\,C'_{15}\,\boldsymbol{\sigma}_1+G^V_E(q^2)\,C'_{16}\\ &\quad\times(\tau_{1,z}-\tau_{2,z})\,\boldsymbol{\sigma}_1\big]\times\mathbf{q}+1\rightleftharpoons 2. \qquad (2.21)\end{aligned}$$

The expression above for $\mathbf{j}^{(1)}_{\rm a,min}$ is the Fierz-transformed version of the current given in Eq. (3.11) of Ref. [5] (see Appendix A for a derivation). We note that the first three terms in Eq. (2.20) agree with the first line of Eq. (5.3) of Kölling *et al.* [8], while the term proportional to C_5 differs by the isoscalar piece, which, however, can be absorbed in a redefinition of C'_{15}. The LECs $C_1,\ldots,C_7$, which also enter the two-nucleon contact potential, have been constrained by fitting np and pp elastic scattering data and the deuteron binding energy. We take their values from the Machleidt and Entem 2011 review paper [20]. The LECs C'_{15} and C'_{16} (and d'_8, d'_9, and d'_{21} below) are determined by fitting measured photonuclear observables of the $A = 2$ and 3 systems, as discussed in Sec. IV. Finally, we observe that there is no *a priori* justification for the use of G^S_E and G^V_E (or G^S_M and G^V_M) in the nonminimal contact current, and these form factors are included in order to provide a reasonable fall-off with increasing q^2 for the strength of this current.

The isovector (IV) OPE current at N3LO is given by

$$\begin{aligned}\mathbf{j}^{(1)}_{\rm b,IV} &= i\,e\,\frac{g_A}{F_\pi^2}\,\frac{G_{\gamma N\Delta}(q^2)}{\mu_{\gamma N\Delta}}\,\frac{\boldsymbol{\sigma}_2\cdot\mathbf{k}_2}{\omega^2_{k_2}}\,[d'_8\tau_{2,z}\,\mathbf{k}_2\\ &\quad-d'_{21}(\boldsymbol{\tau}_1\times\boldsymbol{\tau}_2)_z\,\boldsymbol{\sigma}_1\times\mathbf{k}_2]\times\mathbf{q}+1\rightleftharpoons 2, \qquad (2.22)\end{aligned}$$

and it depends on the two (unknown) LECs, d'_8 and d'_{21}. They can be related [5] to the N-Δ transition axial coupling constant and magnetic moment (denoted as $\mu_{\gamma N\Delta}$) in a resonance saturation picture, which justifies the use of the $\gamma N\Delta$ electromagnetic form factor for this term. It is parametrized as

$$G_{\gamma N\Delta}(q^2) = \frac{\mu_{\gamma N\Delta}}{\left(1+q^2/\Lambda^2_{\Delta,1}\right)^2\sqrt{1+q^2/\Lambda^2_{\Delta,2}}}, \qquad (2.23)$$

where $\mu_{\gamma N\Delta}$ is taken as $3\mu_N$ from an analysis of γN data in the Δ-resonance region [21]. This analysis also gives $\Lambda_{\Delta,1} = 0.84$ GeV and $\Lambda_{\Delta,2} = 1.2$ GeV. The isoscalar (IS) piece of the OPE current depends on the LEC d'_9 mentioned earlier,

$$\mathbf{j}^{(1)}_{\rm b,IS} = i\,e\,\frac{g_A}{F_\pi^2}\,d'_9\,G_{\gamma\pi\rho}(q^2)\,\boldsymbol{\tau}_1\cdot\boldsymbol{\tau}_2\,\frac{\boldsymbol{\sigma}_2\cdot\mathbf{k}_2}{\omega^2_{k_2}}\,\mathbf{k}_2\times\mathbf{q}+1\rightleftharpoons 2, \qquad (2.24)$$

and, again in a resonance saturation picture, reduces to the well-known $\gamma\pi\rho$ current [5]. Accordingly, we have accounted for the q^2 fall-off of the electromagnetic vertex by including a $\gamma\pi\rho$ form factor, which in vector-meson dominance is parametrized as

$$G_{\gamma\pi\rho}(q^2) = \frac{1}{1+q^2/m^2_\omega}, \qquad (2.25)$$

where m_ω is the ω-meson mass. We can now clarify the differences in these tree-level currents as reported here and in Ref. [8]. We first note that the relations between the primed d'_i and d_i in Ref. [5] should have read $d'_8 = -8d_8$, $d'_9 = -8d_9$, and $d'_{21} = 2d_{21} - d_{22}$. The term proportional to d_{22} originates from the Lagrangian,

$$\text{term} \propto d_{22} = \frac{2e}{F_\pi}d_{22}\,N^\dagger S^\mu[\partial^\nu(\boldsymbol{\tau}\times\boldsymbol{\pi})_z\,F_{\mu\nu}]N. \qquad (2.26)$$

Kölling *et al.* [8] integrate it by parts to obtain

$$\begin{aligned}\text{term} \propto d_{22} &= -\frac{2\,e}{F_\pi}\,d_{22}[(\partial^\nu N)^\dagger S^\mu\,(\boldsymbol{\tau}\times\boldsymbol{\pi})_z\,F_{\mu\nu}N\\ &\quad+N^\dagger S^\mu(\boldsymbol{\tau}\times\boldsymbol{\pi})_z\,F_{\mu\nu}(\partial^\nu N)], \qquad (2.27)\end{aligned}$$

while the authors of Ref. [5] use the equations of motion for the electromagnetic field tensor at leading order, $\partial^\nu F_{\mu\nu} = 0$, to express it as

$$\text{term} \propto d_{22} = \frac{2\,e}{F_\pi}\,d_{22}\,N^\dagger\,S^\mu\,F_{\mu\nu}\,(\boldsymbol{\tau}\times\partial^\nu\boldsymbol{\pi})_z\,N. \qquad (2.28)$$

These two different treatments lead to the d_{22} current as given in Refs. [5,8]. They differ by a term proportional to $(\boldsymbol{\sigma}_1\times\mathbf{q})\times\mathbf{q}$, which does not contribute to the magnetic moment ($M1$) operator $\boldsymbol{\mu} = -(i/2)\,\boldsymbol{\nabla}_q\times\mathbf{j}|_{q=0}$ [5]. Similarly, the term proportional to $f_5(q)$ in Eq. (4.28) of Ref. [8] does not give any contribution to $\boldsymbol{\mu}$, since $f_5(q)\propto q^2$ for small q. The term proportional to $f_6(q)$ is included in Eq. (2.7) provided $g_A^2 \longrightarrow g_A^2\left(1-d_{18}\,m_\pi^2/g_A\right)$. The value adopted here for g_A is obtained from two-nucleon scattering data (Sec. IV). Therefore, for processes induced by $M1$ transitions, such as the nd and n^3He radiative captures at thermal neutron energies studied in Ref. [22] or the magnetic scattering under consideration in this work, the differences above are irrelevant.

The one-loop TPE currents, diagrams (c)–(k) of Fig. 2, are written as

$$\mathbf{j}^{(1)}_{\rm loop} = -i\, e\, G^V_E(q^2)\,(\boldsymbol{\tau}_1 \times \boldsymbol{\tau}_2)_z\, \boldsymbol{\nabla}_k\, F_1(k) + i\, e\, G^V_E(q^2)\,\tau_{2,z} \times \left[F_0(k)\,\boldsymbol{\sigma}_1 - F_2(k)\,\frac{\mathbf{k}\,\boldsymbol{\sigma}_1\cdot\mathbf{k}}{k^2}\right]\times \mathbf{q} + 1 \rightleftharpoons 2, \quad (2.29)$$

where the functions $F_i(k)$ are

$$F_0(k) = \frac{g_A^2}{8\,\pi^2 F_\pi^4}\left[1 - 2\,g_A^2 + \frac{8\,g_A^2\,m_\pi^2}{k^2+4\,m_\pi^2} + G(k)\left[2 - 2\,g_A^2 - \frac{4\left(1+g_A^2\right)m_\pi^2}{k^2+4\,m_\pi^2} + \frac{16\,g_A^2\,m_\pi^4}{\left(k^2+4\,m_\pi^2\right)^2}\right]\right], \quad (2.30)$$

$$F_1(k) = \frac{1}{96\,\pi^2\,F_\pi^4}\,G(k)\left[4m_\pi^2\left(1+4g_A^2-5g_A^4\right) + k^2\left(1+10g_A^2-23g_A^4\right) - \frac{48\,g_A^4 m_\pi^4}{4\,m_\pi^2+k^2}\right], \quad (2.31)$$

$$F_2(k) = \frac{g_A^2}{8\,\pi^2 F_\pi^4}\left[2 - 6\,g_A^2 + \frac{8\,g_A^2\,m_\pi^2}{k^2+4\,m_\pi^2} + G(k)\left[4\,g_A^2 - \frac{4\left(1+3\,g_A^2\right)m_\pi^2}{k^2+4\,m_\pi^2} + \frac{16\,g_A^2\,m_\pi^4}{\left(k^2+4\,m_\pi^2\right)^2}\right]\right], \quad (2.32)$$

and the loop function $G(k)$ is defined as

$$G(k) = \frac{\sqrt{4\,m_\pi^2+k^2}}{k}\,\ln\frac{\sqrt{4\,m_\pi^2+k^2}+k}{\sqrt{4\,m_\pi^2+k^2}-k}. \quad (2.33)$$

The expression above results from expanding $\mathbf{j}^{(1)}_{\rm loop}(\mathbf{q},\mathbf{k})$ in a power series in $\mathbf{q}$ as $\mathbf{j}^{(1)}_{\rm loop}(\mathbf{q},\mathbf{k}) = \mathbf{j}^{(1)}_{\rm loop}(0,\mathbf{k}) - i\,\mathbf{q}\times\boldsymbol{\mu}^{(0)}(\mathbf{k}) + \cdots$, where $\boldsymbol{\mu}^{(0)}$ is the magnetic dipole operator, and $\mathbf{j}^{(1)}_{\rm loop}(0,\mathbf{k})$, which corresponds to the first term in Eq. (2.29), satisfies current conservation with the TPE potential $v^{(2)}_{2\pi}(\mathbf{k})$ (of order Q^2), since

$$\left[v^{(2)}_{2\pi}(\mathbf{k}),\,\rho^{(-3)}\right] = e\left[v^{(2)}_{2\pi}(\mathbf{k}-\mathbf{q}/2),\,e_{N,1}\right] + 1 \rightleftharpoons 2 \simeq -i\,e\,(\boldsymbol{\tau}_1\times\boldsymbol{\tau}_2)_z\,\mathbf{q}\cdot\boldsymbol{\nabla}_k F_1(k) + 1 \rightleftharpoons 2 \quad (2.34)$$

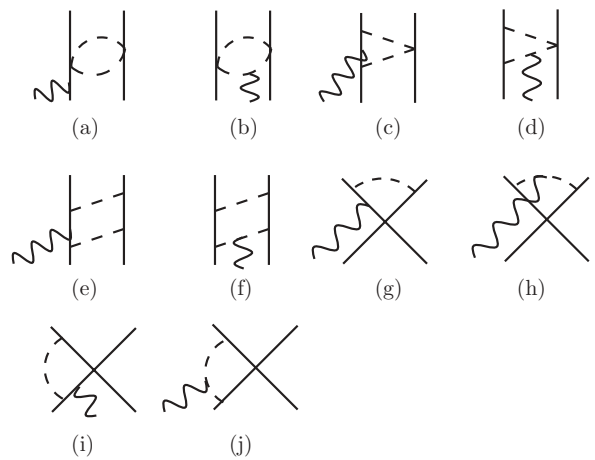

FIG. 3. Diagrams illustrating two-body charge operators entering at order $n = 1$ or eQ. Nucleons, pions, and photons are denoted by the solid, dashed, and wavy lines, respectively. Only one among the possible time orderings is shown.

to leading order in $\mathbf{q}$. In fact, the current $\mathbf{j}^{(1)}_{\rm loop}(0,\mathbf{k})$ is proportional to the electric dipole operator, and it does not contribute to elastic electromagnetic transitions, such as those of interest here.

Finally, we note that a more careful analysis, detailed in Appendix B, of the loop short-range currents corresponding to diagrams (h)–(k) in Fig. 2 shows that they vanish, in contrast to that which was reported in Ref. [5] and in agreement with the result of Ref. [8].

B. Charge operators at order $n = 1$ (eQ)

The two-body charge operators at one loop (N4LO) are illustrated in Fig. 3 and have been derived in Ref. [6]. The contributions from diagrams of type (a) and (b) and (g) and (h) vanish, and after carrying out the loop integrations (discussed in Appendix C), those from diagrams of type (c)–(f) and (i) and (j) read

$$\rho^{(1)}_{\rm c} = -e\,\frac{1}{2\,\pi}\,\frac{g_A^2}{F_\pi^4}\,G^V_E(q^2)\,\tau_{2,z}\int_0^{1/2} dx\left[4\,L(x,k_2) - \frac{m_\pi^2}{L(x,k_2)}\right] + 1 \rightleftharpoons 2, \quad (2.35)$$

$$\rho^{(1)}_{\rm d} = e\,\frac{1}{2\,\pi}\,\frac{g_A^2}{F_\pi^4}\,G_\pi(q^2)\,\tau_{2,z}\int_0^{1/2} dx\left[4\,L(x,k_1) - \frac{m_\pi^2}{L(x,k_1)}\right] + 1 \rightleftharpoons 2, \quad (2.36)$$

$$\rho^{(1)}_{\rm e}(\nu) = -e\,\frac{1}{16\,\pi}\,\frac{g_A^2}{F_\pi^4}\,G^V_E(q^2)\int_0^{1/2} dx\left[[4\,\tau_{2,z} + \nu\,(\boldsymbol{\tau}_1\times\boldsymbol{\tau}_2)_z]\left[-24\,L(x,k_2) + \frac{k_2^2+8\,m_\pi^2}{L(x,k_2)} + \frac{m_\pi^4}{L^3(x,k_2)}\right] + [4\,\tau_{1,z} - \nu\,(\boldsymbol{\tau}_1\times\boldsymbol{\tau}_2)_z]\frac{(\boldsymbol{\sigma}_2\times\mathbf{k}_2)\cdot(\boldsymbol{\sigma}_1\times\mathbf{k}_2)}{L(x,k_2)}\right] + 1 \rightleftharpoons 2, \quad (2.37)$$

$$\rho^{(1)}_{\rm f} = -e\frac{1}{8\,\pi}\,\frac{g_A^4}{F_\pi^4}\,G_\pi(q^2)\int_0^1 dx\,x\int_{-1/2}^{1/2} dy\left[-2\,\tau_{1,z}\left[-15\,\lambda(x,y) + \frac{1}{\lambda(x,y)}[3\,\mathbf{A}\cdot(\mathbf{B}+\mathbf{C}) + (\mathbf{A}+\mathbf{B})\cdot(\mathbf{A}+\mathbf{C}) + (\boldsymbol{\sigma}_1\times\mathbf{A})\cdot(\boldsymbol{\sigma}_2\times\mathbf{A}) - (\boldsymbol{\sigma}_1\times\mathbf{A})\cdot(\boldsymbol{\sigma}_2\times\mathbf{C}) - (\boldsymbol{\sigma}_1\times\mathbf{B})\cdot(\boldsymbol{\sigma}_2\times\mathbf{A}) + (\boldsymbol{\sigma}_1\times\mathbf{B})\cdot(\boldsymbol{\sigma}_2\times\mathbf{C})\right]$$

$$+\frac{1}{\lambda^3(x,y)}[(\mathbf{A}\cdot\mathbf{B})(\mathbf{A}\cdot\mathbf{C})+\boldsymbol{\sigma}_1\cdot(\mathbf{A}\times\mathbf{B})\,\boldsymbol{\sigma}_2\cdot(\mathbf{A}\times\mathbf{C})]\Big]+\frac{1}{\lambda(x,y)}(\boldsymbol{\tau}_1\times\boldsymbol{\tau}_2)_z\Big[-3\,\boldsymbol{\sigma}_2\cdot(\mathbf{A}\times\mathbf{C})$$
$$-\mathbf{B}\cdot(\boldsymbol{\sigma}_2\times\mathbf{A})+(\mathbf{A}+\mathbf{B})\cdot(\boldsymbol{\sigma}_2\times\mathbf{C})-\frac{1}{\lambda^2(x,y)}\mathbf{A}\cdot\mathbf{B}\,\boldsymbol{\sigma}_2\cdot(\mathbf{A}\times\mathbf{C})\Big]\Big]+1\rightleftharpoons 2, \tag{2.38}$$

$$\rho_{\rm i}^{(1)}=e\,\frac{1}{\pi}\,\frac{g_A^2}{F_\pi^2}\,C_T\,G_E^V(q^2)\,\tau_{1,z}\,\boldsymbol{\sigma}_1\cdot\,\boldsymbol{\sigma}_2\,m_\pi+1\rightleftharpoons 2, \tag{2.39}$$

$$\rho_{\rm j}^{(1)}=-e\,\frac{1}{\pi}\,\frac{g_A^2}{F_\pi^2}\,C_T\,G_\pi(q^2)\,\tau_{1,z}\int_0^{1/2}dx\Big[\frac{3\,L^2(x,q)-m_\pi^2}{L(x,q)}\boldsymbol{\sigma}_1\cdot\boldsymbol{\sigma}_2-\frac{1/4-x^2}{L(x,q)}\,\boldsymbol{\sigma}_1\cdot\mathbf{q}\,\boldsymbol{\sigma}_2\cdot\mathbf{q}\Big]+1\rightleftharpoons 2, \tag{2.40}$$

where we have defined

$$L^2(x,p)=(1/4-x^2)\,\mathbf{p}^2+m_\pi^2, \tag{2.41}$$
$$\lambda^2(x,y)=x\,\mathbf{q}^2/4-[x\,y\,\mathbf{q}-(1-x)\,\mathbf{k}]^2+(1-x)\,\mathbf{k}^2+m_\pi^2, \tag{2.42}$$
$$\mathbf{A}=-x\,(y\,\mathbf{q}+\mathbf{k}), \tag{2.43}$$
$$\mathbf{B}=(1-2\,x\,y)\,\mathbf{q}/2+(1-x)\,\mathbf{k}, \tag{2.44}$$
$$\mathbf{C}=-(1+2\,x\,y)\,\mathbf{q}/2+(1-x)\,\mathbf{k}. \tag{2.45}$$

It is easily verified that the charge operators (c) + (d), (e) + (f), and (i) + (j) vanish at $\mathbf{q}=0$. Finally, we note that the form of the operator (e) depends on the off-the-energy-shell prescription adopted for the nonstatic corrections to the TPE potential. As in the OPE case, however, these different forms for the TPE nonstatic potential and accompanying charge operator are unitarily equivalent [6]; in particular, $\rho_{\rm e}^{(1)}(\nu)=\rho_{\rm e}^{(1)}(0)+[\rho^{(-3)},i\,U^{(1)}(\nu)]$. In closing, we note that the reanalysis, outlined in Appendix B, of the loop corrections to the short-range charge operators illustrated in panels (g)–(j) has led to expressions which are different from those reported originally in Ref. [5]. They also differ from those in Ref. [8].

III. CALCULATION

The deuteron charge (G_C), magnetic (G_M), and quadrupole (G_Q) form factors are obtained from Ref. [23]

$$G_C(q)=\frac{1}{3}\sum_{M=\pm1,0}\langle d;M|\rho(q\,\hat{\mathbf{z}})|d;M\rangle, \tag{3.1}$$

$$G_M(q)=\frac{1}{\sqrt{2\,\eta}}\,{\rm Im}[\langle d;1|j_y(q\,\hat{\mathbf{z}})|d;0\rangle], \tag{3.2}$$

$$G_Q(q)=\frac{1}{2\,\eta}[\langle d;0|\rho(q\,\hat{\mathbf{z}})|d;0\rangle-\langle d;1|\rho(q\,\hat{\mathbf{z}})|d;1\rangle], \tag{3.3}$$

where $|d;M\rangle$ is the deuteron state with spin projection $J_z=M$, ρ and j_y denote, respectively, the charge operator and y component of the current operator, the momentum transfer $\mathbf{q}$ is taken along the z axis (the spin quantization axis), and $\eta=(q/2\,m_d)^2$ (where m_d is the deuteron mass). They are normalized as

$$G_C(0)=1,\quad G_M(0)=(m_d/m_N)\,\mu_d,\qquad G_Q(0)=m_d^2\,Q_d, \tag{3.4}$$

where μ_d and Q_d are the deuteron magnetic moment (in units of μ_N) and quadrupole moment, respectively. Expressions relating the form factors to the measured structure functions A and B and tensor polarization T_{20} are given in Ref. [23]. The calculations are carried out in momentum space [23] with techniques similar to those described in some detail below for the trinucleons.

The charge and magnetic form factors of the trinucleons are derived from

$$F_C(q)=\frac{1}{Z}\,\langle+|\rho(q\,\hat{\mathbf{z}})|+\rangle, \tag{3.5}$$

$$F_M(q)=-\frac{2\,m_N}{q}\,{\rm Im}[\langle-|j_y(q\,\hat{\mathbf{z}})|+\rangle], \tag{3.6}$$

with the normalizations

$$F_C(0)=1,\quad F_M(0)=\mu, \tag{3.7}$$

where μ is the magnetic moment (in units of μ_N). Here $|\pm\rangle$ represent either the ^{3}He state or ^{3}H state in spin projections $J_z=\pm1/2$. In momentum space, the one-body electromagnetic operators in Sec. II have the generic form

$$O_{\rm 1b}(\mathbf{q})=\sum_{\rm cyclic\,l,m,n}\bar{\delta}(\mathbf{k}_l-\mathbf{q})\,\bar{\delta}(\mathbf{k}_m)\,\bar{\delta}(\mathbf{k}_n)\,O_{\rm 1b}(\mathbf{k}_l,\mathbf{K}_l), \tag{3.8}$$

and their matrix elements can be written as

$$\langle O_{\rm 1b}(\mathbf{q})\rangle=\sum_{\rm cyclic\,l,m,n}\int_{\mathbf{p}_l,\mathbf{p}_m,\mathbf{p}_n}\psi^\dagger_{M'}(\mathbf{p}_l+\mathbf{q}/2,\mathbf{p}_m,\mathbf{p}_n)\times O_{\rm 1b}(\mathbf{q},\mathbf{p}_l)\,\psi_M(\mathbf{p}_l-\mathbf{q}/2,\mathbf{p}_m,\mathbf{p}_n), \tag{3.9}$$

where we have defined

$$\int_{\mathbf{p}_i}=\int\frac{d\mathbf{p}_i}{(2\,\pi)^3}\quad\text{and}\quad\bar{\delta}(\cdots)=(2\,\pi)^3\,\delta(\cdots). \tag{3.10}$$

For an assigned configuration $(\mathbf{p}_l,\mathbf{p}_m,\mathbf{p}_n)$, the wave functions are expanded on a basis of 8×3 spin-isospin states for the three nucleons as

$$\psi(\mathbf{p}_l,\mathbf{p}_m,\mathbf{p}_n)=\sum_{a=1}^{24}\psi_a(\mathbf{p}_l,\mathbf{p}_m,\mathbf{p}_n)\,|a\rangle, \tag{3.11}$$

where the components ψ_a are complex functions and the basis states (for ^{3}H, for example) $|a\rangle=|(p\uparrow)_1,(n\uparrow)_2,(n\uparrow)_3\rangle$, $|(n\uparrow)_1,(p\uparrow)_2,(n\uparrow)_3\rangle$, and so on. The spin-isospin algebra

for the overlaps,

$$\psi^\dagger\, O\, \psi = \sum_{a,b=1}^{24} \psi_a^*\, O_{ab}\, \psi_b, \tag{3.12}$$

is carried out with the techniques developed in Ref. [24]. Monte Carlo (MC) methods are used to evaluate the integrations in Eq. (3.9) by sampling momenta from a (normalized) probability density $|\psi_M(\mathbf{p}_l, \mathbf{p}_m, \mathbf{p}_n)|^2$ according to the Metropolis algorithm.

The two-body operators in Sec. II have the momentum-space representation

$$O_{2\mathrm{b}}(\mathbf{q}) = \sum_{\text{cyclic}\, l,m,n} \bar{\delta}(\mathbf{K}_{lm} - \mathbf{q})\, \bar{\delta}(\mathbf{k}_n) \times O_{2\mathrm{b}}(\mathbf{K}_{lm}/2 + \mathbf{k}_{lm}, \mathbf{K}_{lm}/2 - \mathbf{k}_{lm}), \tag{3.13}$$

where the momenta $\mathbf{K}_{lm} = \mathbf{k}_l + \mathbf{k}_m$ and $\mathbf{k}_{lm} = (\mathbf{k}_l - \mathbf{k}_m)/2$. These operators have power-law behavior at large momenta and need to be regularized. This is accomplished by introducing a momentum cutoff function of the form

$$C_\Lambda(k_{lm}) = \mathrm{e}^{-(k_{lm}/\Lambda)^4}, \tag{3.14}$$

with the parameter Λ in the range 500–600 MeV (see discussion in Sec. IV). The matrix elements are expressed as

$$\langle O_{2\mathrm{b}}(\mathbf{q})\rangle = \sum_{\text{cyclic}\, l,m,n} \int_{\mathbf{k}_{lm}} \int_{\mathbf{p}_l,\mathbf{p}_m,\mathbf{p}_n} \psi^\dagger_{M'}(\mathbf{p}_l + \mathbf{q}/4 + \mathbf{k}_{lm}/2, \mathbf{p}_m + \mathbf{q}/4 - \mathbf{k}_{lm}/2, \mathbf{p}_n)\, C_\Lambda(k_{lm}) O_{2\mathrm{b}}(\mathbf{q}, \mathbf{k}_{lm}) \times \psi_M(\mathbf{p}_l - \mathbf{q}/4 - \mathbf{k}_{lm}/2, \mathbf{p}_m - \mathbf{q}/4 + \mathbf{k}_{lm}/2, \mathbf{p}_n). \tag{3.15}$$

The spin-isospin algebra is handled as above, while the multidimensional integrations are efficiently done by a combination of MC and standard quadrature techniques. We write

$$\langle O_{2\mathrm{b}}(\mathbf{q})\rangle = \int d\hat{\mathbf{k}} \int_{\mathbf{p}_l,\mathbf{p}_m,\mathbf{p}_n} F(\hat{\mathbf{k}}, \mathbf{p}_l, \mathbf{p}_m, \mathbf{p}_n) \simeq \frac{1}{N_c} \sum_{c=1}^{N_c} \frac{F(c)}{W(c)}, \tag{3.16}$$

where c denotes configurations $(\hat{\mathbf{k}}, \mathbf{p}_l, \mathbf{p}_m, \mathbf{p}_n)$ (for total number N_c) sampled with the Metropolis algorithm from the probability density $W(c) = |\psi_M(\mathbf{p}_l, \mathbf{p}_m, \mathbf{p}_n)|^2/(4\pi)$, i.e., uniformly over the $\hat{\mathbf{k}}$ directions. For each such configuration c, the function F is obtained by Gaussian integration over the magnitude k_{lm} (as well as the parameters x and y for the case of the charge operators at one loop):

$$F(c) = \sum_{\text{cyclic}\, l,m,n} \frac{1}{(2\pi)^3} \int_0^\infty dk_{lm}\, k_{lm}^2 \sum_{a,b=1}^{24} \psi_a^*(\cdots k_{lm}\hat{\mathbf{k}} \cdots) \times O_{2\mathrm{b},ab}(\mathbf{q}, k_{lm}\hat{\mathbf{k}})\, \psi_b(\cdots k_{lm}\hat{\mathbf{k}} \cdots). \tag{3.17}$$

Convergence in these Gaussian integrations requires of the order of 20–30 points, in the case of k_{lm} distributed over a nonuniform grid up to $2\,\Lambda$ or so, while N_c of the order of 100 000 is sufficient to reduce the statistical errors in the MC integrations, which are of the order of a few percent at the highest q values (and considerably smaller at lower q). These MC errors are further reduced by taking appropriate linear combinations of the matrix elements of the electromagnetic operators using different $\hat{\mathbf{q}}$ directions and different spin projections for the initial and final states. The trinucleons wave functions are obtained with the hyperspherical harmonics (HH) expansion discussed in Refs. [25–27]. This method can be applied in either coordinate or momentum space. Below, we briefly review its momentum-space implementation.

A. The hyperspherical harmonics method in momentum space

The trinucleon wave functions with total angular momentum $J J_z$ are written as

$$|\psi^{J J_z}\rangle = \sum_\mu c_\mu \left|\psi_\mu^{J J_z}\right\rangle, \tag{3.18}$$

where $|\psi_\mu^{J J_z}\rangle$ is a suitable complete set of states and μ is an index denoting the set of quantum numbers necessary to specify the basis elements (see below). By applying the Rayleigh-Ritz variational principle, the problem of determining c_μ and the ground-state energy E_0 of the system is reduced to a generalized eigenvalue problem.

In momentum space we define the Jacobi momenta as

$$\mathbf{k}_{2p} = (\mathbf{p}_j - \mathbf{p}_i)/\sqrt{2}, \quad \mathbf{k}_{1p} = \sqrt{2/3}[\mathbf{p}_k - (\mathbf{p}_i + \mathbf{p}_j)/2], \tag{3.19}$$

where $\mathbf{p}_i$ denotes the momentum of nucleon i and p specifies a given permutation of the three nucleons, with $p = 1$ corresponding to the ordering 1, 2, 3. We introduce a hypermomentum K and a set of angular and hyperangular variables as

$$K = \left(k_{1p}^2 + k_{2p}^2\right)^{1/2}, \quad \Omega_p^{(K)} = [\hat{\mathbf{k}}_{2p}, \hat{\mathbf{k}}_{1p}; \phi_p], \tag{3.20}$$

where $\tan\phi_p = k_{1p}/k_{2p}$. In terms of these variables, the basis functions $|\psi_\mu^{J J_z}\rangle$ are defined as

$$\left|\psi_\mu^{J J_z)}\right\rangle = g_{G\,l}(K)\mathcal{Y}_{\{G\}}(\Omega^{(K)}), \tag{3.21}$$

where the $\mathcal{Y}_{\{G\}}(\Omega^{(K)})$ are written as [28]

$$\mathcal{Y}_{\{G\}}(\Omega^{(K)}) = \sum_{p=1}^{3} \left[Y_{[G]}^{L L_z}\left(\Omega_p^{(K)}\right) \otimes \left[S_2 \otimes \frac{1}{2} \right]_{S S_z} \right]_{J J_z} \times \left[T_2 \otimes \frac{1}{2} \right]_{T T_z}, \tag{3.22}$$

and the sum is over the three even permutations. The spins (isospins) of nucleons i and j are coupled to S_2 (T_2), which is then coupled to the spin (isospin) of the third nucleon to give a state with total spin S (isospin $T T_z$). The total orbital angular momentum L and total spin S are coupled to the total angular momentum $J J_z$. The functions $Y_{[G]}^{L L_z}(\Omega_p^{(K)})$ with definite values of $L L_z$ are the HH functions and are written as [25]

$$Y_{[G]}^{L L_z}\left(\Omega_p^{(K)}\right) = \left[Y_{\ell_2}\left(\hat{\mathbf{k}}_{2p}\right) \otimes Y_{\ell_1}\left(\hat{\mathbf{k}}_{1p}\right) \right]_{L L_z} N_{[G]} (\cos\phi_p)^{\ell_2} \times (\sin\phi_p)^{\ell_1}\, P_n^{\ell_1+\frac{1}{2},\ell_2+\frac{1}{2}}(\cos 2\phi_p), \tag{3.23}$$

where $Y_{\ell_1}(\hat{\mathbf{k}}_{1p})$ and $Y_{\ell_2}(\hat{\mathbf{k}}_{2p})$ are spherical harmonics, $N_{[G]}$ is a normalization factor, and $P_n^{\ell_1+\frac{1}{2},\ell_2+\frac{1}{2}}(\cos 2\phi_p)$ denotes the Jacobi polynomial of degree n. The grand angular quantum number G is defined as $G = 2n + \ell_1 + \ell_2$. The subscripts $\{G\}$ and $[G]$ in Eqs. (3.21)–(3.23) stand, respectively, for $\{G\} \equiv \{\ell_1, \ell_2, L, S_2, T_2, S, T; n\}$ and $[G] \equiv [\ell_1, \ell_2; n]$, and μ in Eq. (3.18) stands for $\mu \equiv \{G\}l$. Finally, the functions $g_{Gl}(K)$ in Eq. (3.21) are defined as

$$g_{Gl}(K) = \frac{(-i)^G}{K^2} \int_0^\infty d\rho\, \rho^3\, J_{G+2}(K\rho)\, f_l(\rho), \quad (3.24)$$

where $J_{G+2}(K\rho)$ are Bessel functions and the functions $f_l(\rho)$ are related to Laguerre polynomials $L_l^{(5)}(\gamma\rho)$ via

$$f_l(\rho) = \gamma^3 \sqrt{l!/(l+5)!}\; L_l^{(5)}(\gamma\rho)\, \mathrm{e}^{-\gamma\rho/2}. \quad (3.25)$$

The nonlinear parameter γ is variationally optimized. With this form of $f_l(\rho)$, the corresponding functions $g_{Gl}(K)$ can easily be calculated, and are explicitly given in Ref. [26]. The form adopted for $g_{Gl}(K)$ is such that the momentum-space basis is simply the Fourier transform of the coordinate-space one [27].

IV. RESULTS

In Sec. IV A, we discuss various strategies for the determination of the unknown LECs d_8', d_9', d_{21}', C_{15}', and C_{16}' entering the current operator at N3LO. In contrast, the charge operator up to N4LO only depends on the nucleon axial coupling constant g_A, pion decay amplitude F_π, and nucleon mass and magnetic moments. The values adopted in the present work for g_A and F_π are, respectively, 1.28 and 184.6 MeV, which give a πN coupling constant ($g_{\pi NN}$) of 13.6, as obtained in analyses of NN elastic scattering data at energies below the pion production threshold [29]. The two-body operators are regularized via the cutoff function in Eq. (3.14), and Λ values of 500 and 600 MeV are considered.

In Secs. IV B and IV C we present results, respectively, for the deuteron $A(q)$ and $B(q)$ structure functions and tensor polarization $T_{20}(q)$ and for the charge and magnetic form factors of ^{3}H and ^{3}He, along with results for the static properties of these few-nucleon systems including the deuteron quadrupole moment, the deuteron and trinucleon charge, and magnetic radii and magnetic moments. The $A = 2$ calculations use either the Argonne v_{18} (AV18) [19] or chiral potentials at order Q^4 with cutoff set at 500 MeV (N3LO) or 600 MeV (N3LO*) [20]. Of course, the $A = 3$ calculations also include three-nucleon potentials—the Urbana-IX model [30] in combination with AV18 and the chiral N2LO potential [31] in combination with either the N3LO or N3LO*. The LECs c_D and c_E (in standard notation) in the chiral three-nucleon potential have been constrained by reproducing the ^{3}H-^{3}He binding energies and the tritium Gamow-Teller matrix element [32] in each case. With the AV18/UIX Hamiltonian, the ^{3}H and ^{3}He binding energies are found to be 8.487 and 7.747 MeV, respectively.

The calculations are carried out in configuration space in Sec. IV A and in momentum space—with the methods outlined in Sec. III—in Secs. IV B and IV C. We have checked that the r- and p-space versions of the computer codes produce identical results up to to tiny differences due to numerics and to numerically nonequivalent implementations of the momentum cutoff function in Eq. (3.14) in these r- and p-space calculations. The hadronic electromagnetic form factors entering the one- and two-body charge and current operators are those specified in Sec. II. The matrix elements of these operators are evaluated in the Breit frame with Monte Carlo methods. The number of sampled configurations is of the order of 10^6 for the deuteron and 10^5 for the $A = 3$ systems. The statistical errors, which are not shown in the results that follow, are typically $\lesssim 1\%$ over the whole momentum-transfer range, and in fact they are much less than 1% for $q \lesssim 2$ fm^{-1}.

A. Determination of the LECs

As already remarked, the LECs C_i, $i = 1, \ldots, 7$, in the minimal contact current, corresponding to Λ cutoffs of 500 and 600 MeV, are taken from fits to NN scattering data [20]. In reference to the LECs entering the OPE and nonminimal contact currents at N3LO, it is convenient to introduce the adimensional set $d_i^{S,V}$ (in units of the cutoff Λ) as

$$\begin{aligned} C_{15}' &= d_1^S/\Lambda^4, \quad d_9' = d_2^S/\Lambda^2, \\ C_{16}' &= d_1^V/\Lambda^4, \quad d_8' = d_2^V/\Lambda^2, \quad d_{21}' = d_3^V/\Lambda^2, \end{aligned} \quad (4.1)$$

where the superscripts S and V characterize the isospin of the associated operator, i.e., whether it is isoscalar or isovector. The isoscalar d_i^S, listed in Table I, have been fixed by reproducing the experimental deuteron magnetic moment μ_d and isoscalar combination μ_S of the trinucleon magnetic moments. The LEC d_1^S multiplying the contact current is rather large, but not unreasonably large, while the LEC d_2^S is quite small. The cumulative contributions to μ_d and μ_S are reported in Table II. The NLO and N3LO-loop magnetic moment operators are isovector, and therefore they do not contribute to these isoscalar observables. At N3LO the only nonvanishing contributions are those associated with the OPE and minimal (min) and nonminimal (nm) contact currents. Of course, the last row in Table II reproduces the experimental values for μ_d and μ_S.

The isovector LEC d_3^V is taken as $d_2^V/4$ by assuming Δ dominance. The three different sets of remaining LECs d_1^V and d_2^V reported in Table III have been determined in the following way. In set I d_1^V and d_2^V have been constrained to reproduce the experimental values of the np radiative capture cross section σ_{np} at thermal neutron energies and the isovector combination μ_V of the trinucleons magnetic moments. This procedure, however, leads to unreasonably large values for both LECs,

TABLE I. Adimensional values of the isoscalar LECs corresponding to cutoffs $\Lambda = 500$ and 600 MeV obtained for the N3LO/N2LO and N3LO*/N2LO* Hamiltonians; the values in parentheses are relative to the AV18/UIX Hamiltonian.

Λ	d_1^S	$d_2^S \times 10$
500	4.072 (2.522)	2.190 (−1.731)
600	11.38 (5.238)	3.231 (−2.033)

TABLE II. Cumulative contributions to the deuteron and trinucleons isoscalar magnetic moments in units of μ_N, corresponding to cutoffs $\Lambda = 500$ and 600 MeV obtained for the N3LO/N2LO and N3LO*/N2LO* Hamiltonians; the contributions in parentheses are relative to the AV18/UIX Hamiltonian. The experimental values for the deuteron and trinucleons isoscalar magnetic moments are $0.8574\mu_N$ and $0.4257\mu_N$, respectively.

Λ	μ_d		μ_S	
	500	600	500	600
LO	0.8543(0.8472)	0.8543(0.8472)	0.4222(0.4104)	0.4220(0.4104)
N2LO	0.8471(0.8400)	0.8474(0.8400)	0.4143(0.4027)	0.4155(0.4027)
N3LO(min)	0.8725(0.8739)	0.8806(0.8760)	0.4501(0.4455)	0.4611(0.4483)
N3LO(nm)	0.8548(0.8593)	0.8538(0.8626)	0.4247(0.4269)	0.4235(0.4313)
N3LO(OPE)	0.8574(0.8574)	0.8574(0.8574)	0.4257(0.4257)	0.4257(0.4257)

and it is clearly unacceptable. In particular, it makes the contributions of the associated magnetic dipole operators unnaturally large and, as shown in Table IV, totally spoils the expected convergence pattern. This pathology is especially severe in the case of the AV18/UIX Hamiltonian model.

In sets II and III d_2^V is assumed to be saturated by the Δ resonance, i.e.,

$$d_2^V = \frac{4\,\mu_{\gamma N\Delta}\,h_A\,\Lambda^2}{9\,m_N\,(m_\Delta - m_N)}, \tag{4.2}$$

where $m_\Delta - m_N = 294$ MeV, $h_A/F_\pi = f_{\pi N\Delta}/m_\pi$ with $f_{\pi N\Delta}^2/(4\pi) = 0.35$ as obtained by equating the first-order expression of the Δ-decay width to the experimental value, and the transition magnetic moment $\mu_{\gamma N\Delta} = 3\mu_N$ [21]—a similar strategy has been implemented in a number of calculations, based on the χEFT magnetic moment operator derived in Ref. [4], of the np, nd, and n^3He radiative captures and magnetic moments of $A = 2$ and 3 nuclei [33]. On the other hand, the LEC d_1^V multiplying the contact current is fitted to reproduce either σ_{np} in set II or μ_V in set III. Both alternatives still lead to somewhat large values for this LEC, but we find the degree of unnaturalness tolerable in this case. We observe that there are no three-body currents at N3LO [22], and therefore it is reasonable to fix the strength of this $M1$ operator by fitting a three-nucleon observable such as μ_V.

Cumulative contributions to σ_{np} and μ_V are listed in Table IV. At N3LO, we have identified separately those due only to loop currents labeled as N3LO(loop) and those from loop + minimal contact currents labeled as N3LO(min). The experimental values for σ_{np} and μ_V are reproduced with set I, row labeled N3LO(OPE, d_2^V-I), while only σ_{np} or μ_V are reproduced with set II or III, rows labeled N3LO(OPE, d_2^V-II) or N3LO(OPE, d_2^V-III). Indeed, the N3LO(OPE, d_2^V-II or III) results provide predictions for μ_V or σ_{np}, respectively. These predictions are within 3% for μ_V and 1% for σ_{np} of the experimental values, and they exhibit a weak cutoff and Hamiltonian-model dependence.

In Ref. [22] the d_i^S and d_i^V were determined using the same procedure adopted here for set I. However, the values reported in that work are drastically different from those obtained in the present one. These differences are due to several factors: (i) in Ref. [22] the $M1$ operator derived from Eq. (2.29) included an isovector loop correction proportional to the LECs C_S and C_T, which turns out to vanish in a more careful analysis of the relevant diagrams (the loop short-range currents discussed in Appendix B); (ii) in Ref. [22] the values for the LECs $C_1, \ldots, C_7$ were taken from a chiral potential obtained at Q^2 (NLO) [5] rather than at Q^4 (N3LO) [20] as in the present case; and (iii) in Ref. [22] the minimal contact current is the Fierz-transformed version of that given in Eq. (2.20) (see the discussion in Appendix A). However, this Fierz equivalence is spoiled by the regularization procedure, i.e., by the inclusion of the same cutoff function $C_\Lambda(k)$ for both. Hence the contribution of this current in the present work is different from that obtained in Ref. [22].

B. Static properties and form factors of the deuteron

The deuteron root-mean-square charge radius and quadrupole moment, obtained with the chiral and AV18 potentials and cutoff parameters $\Lambda = 500$ and 600 MeV, are listed in Table V. We denote the leading order ($n = -3$ in the notation of Sec. II) term of Eq. (2.5) with LO, the $n = -1$ relativistic correction of Eqs. (2.11) with N2LO, and the $n = 0$ terms of Eqs. (2.12) and of Eqs. (2.13) and (2.14) with N3LO(OPE) and N3LO(ν), respectively. The remaining charge operators at N4LO ($n = 1$), being isovector, do not contribute to these observables (and corresponding form factors). The N3LO or N3LO* and AV18 potentials neglect retardation corrections in their OPE component, which corresponds to setting $\nu = 1/2$ in

TABLE III. Adimensional values of the isovector LECs corresponding to cutoffs $\Lambda = 500$ and 600 MeV obtained for the N3LO/N2LO and N3LO*/N2LO* Hamiltonians; the values in parentheses are relative to the AV18/UIX Hamiltonian. Note that $d_3^V = d_2^V/4$ in all cases; see text for further explanations.

Λ	d_1^V(I)	d_2^V(I)	d_1^V(II)	d_2^V(II)	d_1^V(III)	d_2^V(III)
500	10.36(45.10)	17.42(35.57)	−13.30(−9.339)	3.458	−7.981(−5.187)	3.458
600	41.84(257.5)	33.14(75.00)	−22.31(−11.57)	4.980	−11.69(−1.025)	4.980

TABLE IV. Cumulative contributions to the np radiative capture cross section in millibarns and trinucleon isovector magnetic moments in units of μ_N, corresponding to cutoffs $\Lambda = 500$ and 600 MeV obtained for the N3LO/N2LO and N3LO*/N2LO* Hamiltonians; the contributions in parentheses are relative to the AV18/UIX Hamiltonian. See text for further explanations. The experimental values for the np cross section and trinucleon isovector magnetic moments are 332.6 ± 0.7 mb and $-2.553\,\mu_N$, respectively.

Λ	σ_{np}		μ_V	
	500	600	500	600
LO	305.8(304.6)	304.6(304.6)	−2.193(−2.159)	−2.182(−2.159)
NLO	320.6(319.3)	318.9(320.9)	−2.408(−2.382)	−2.392(−2.413)
N2LO	319.2(317.7)	317.6(319.2)	−2.384(−2.359)	−2.370(−2.390)
N3LO(loop)	321.3(320.9)	320.5(322.4)	−2.430(−2.418)	−2.432(−2.448)
N3LO(min)	321.3(320.9)	320.5(322.4)	−2.413(−2.406)	−2.415(−2.437)
N3LO(nm, d_1^V-I)	315.2(287.4)	305.7(242.7)	−2.297(−1.782)	−2.142(−0.9029)
N3LO(OPE, d_2^V-I)	332.6(332.6)	332.6(332.6)	−2.553(−2.553)	−2.553(−2.553)
N3LO(nm, d_1^V-II)	329.1(328.1)	328.5(326.2)	−2.562(−2.535)	−2.561(−2.506)
N3LO(OPE, d_2^V-II)	332.6(332.6)	332.6(332.6)	−2.612(−2.610)	−2.622(−2.616)
N3LO(nm, d_1^V-III)	326.0(324.9)	324.7(322.7)	−2.502(−2.478)	−2.491(−2.443)
N3LO(OPE, d_2^V-III)	329.4(329.4)	328.8(329.1)	−2.553(−2.553)	−2.553(−2.553)

Eq. (2.15). Note that the isoscalar piece of the N3LO(ν) charge operator scales as $1 - \nu$, and it contributes less than 0.5% of the LO result for $\nu = 1/2$. The N2LO and N3LO corrections to r_d, which is well reproduced by theory, are negligible. The chiral potential predictions for Q_d are within 1% of the experimental value, while the AV18 ones underestimate it by about 2%. Variation of the cutoff in the 500–600 MeV range leads to about 1% (negligible) changes in the N3LO or N3LO* (AV18) results. The LO and N2LO charge operators do not include the cutoff function and the AV18 results are independent of Λ. This is not the case for the results corresponding to the N3LO and N3LO* potentials because of their intrinsic Λ dependence.

The deuteron $A(q)$ structure function and tensor polarization $T_{20}(q)$, obtained at LO and by including corrections up to N3LO in the charge operator, are compared to data in Fig. 4, top panels. In this figure (as well as in those that follow) the momentum-transfer range goes up to $q = 7.5$ fm^{-1}, much beyond the $\simeq$(3–4)m_π upper limit, where one would naively expect this comparison to be meaningful, given that the present theory retains up to TPE mechanisms. On the other hand, we note that the next (nonvanishing) isoscalar contributions only enter at N5LO ($n = 2$) [11], and they are therefore suppressed by two powers of Q relative to those at N3LO.

The $A(q)$ structure function is well reproduced by theory up to $q \simeq 3$ fm^{-1}. At higher momentum transfers, the N3LO results based on AV18 tend to overestimate the data—a feature also seen in the conventional approach of Ref. [23]—while those based on the chiral potentials still provide a good fit to the data. The cutoff dependence is weak at low q but becomes more pronounced as q increases.

Similar considerations hold for the $T_{20}(q)$ observable, although in this case the N3LO results derived from the chiral potentials overpredict the data for $q \gtrsim 3$ fm^{-1}, while those from AV18 fit reasonably well the data up to $q \simeq 4.5$ fm^{-1}. In contrast, the conventional approach [23] (also based on AV18, of course) reproduces very well the measured T_{20} over the whole q range. The OPE charge operator in that work has the same structure as the present N3LO(OPE) one, but it includes a much harder cutoff than adopted here. Furthermore, the calculation of Ref. [23] also retains short-range (isoscalar) mechanisms associated with ρ-meson exchange and $\gamma\pi\rho$ transition, which in χEFT are presumably subsumed in contact operators at N5LO [11]. We note that in both $A(q)$ and $T_{20}(q)$ a small magnetic contribution, discussed separately below, is accounted for.

The charge and quadrupole form factors extracted from the unpolarized and tensor polarized deuteron data are compared to results obtained in LO and by including corrections up to N3LO in Fig. 4, bottom panels. The $G_C(q)$ and $G_Q(q)$ form factors calculated with deuteron wave functions from the chiral potentials are in qualitative agreement with predictions obtained by Phillips [11] at the same chiral order (although the

TABLE V. Cumulative contributions to the deuteron root-mean-square charge radius and quadrupole moment corresponding to cutoffs $\Lambda = 500$ and 600 MeV obtained with the N3LO and N3LO* Hamiltonians; results in parentheses are relative to the AV18 Hamiltonian. The experimental values for r_d and Q_d are 1.9734(44) fm [34] and 0.2859(3) fm^2 [35], respectively.

Λ	r_d (fm)		Q_d (fm^2)	
	500	600	500	600
LO	1.976(1.969)	1.968(1.969)	0.2750(0.2697)	0.2711(0.2697)
N2LO	1.976(1.969)	1.968(1.969)	0.2731(0.2680)	0.2692(0.2680)
N3LO(OPE)	1.976(1.969)	1.968(1.969)	0.2863(0.2818)	0.2831(0.2814)
N3LO($\nu = 1/2$)	1.976(1.969)	1.968(1.969)	0.2851(0.2806)	0.2820(0.2802)

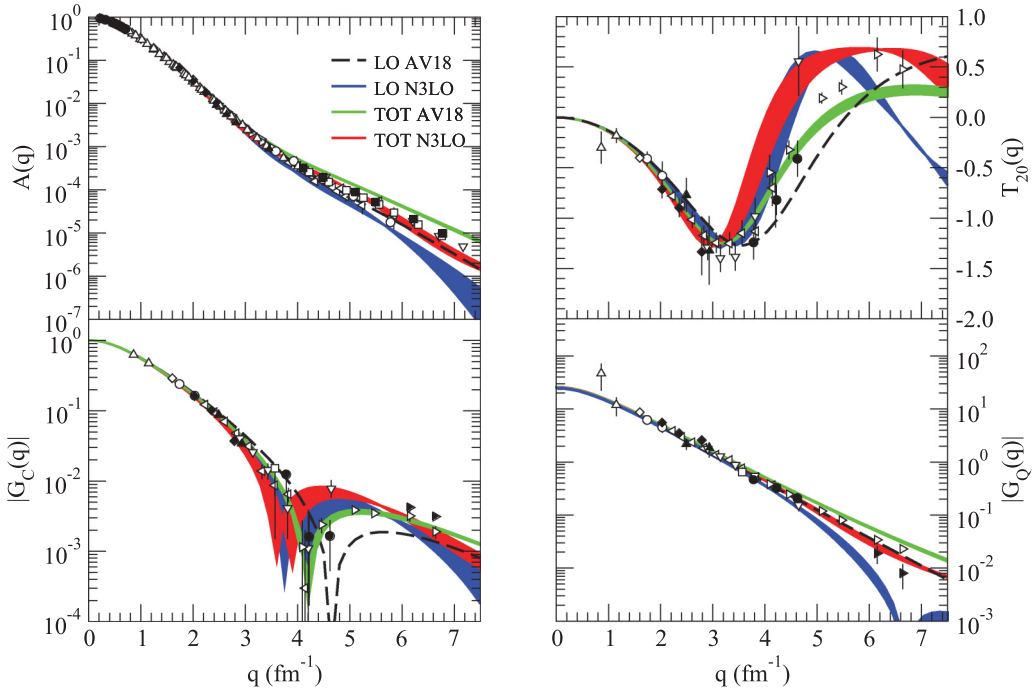

FIG. 4. (Color online) The deuteron $A(q)$ structure function and tensor polarization $T_{20}(q)$ (top panels) and charge and quadrupole form factors $G_C(q)$ and $G_Q(q)$ (bottom panels), obtained at leading order (LO) and with inclusion of charge operators up to N3LO (TOT), compared with experimental data from Refs. [36–57]. Predictions corresponding to $\nu = 1/2$ and cutoffs Λ in the range 500–600 MeV are displayed by the bands.

Q^4 potentials used in that study are from Ref. [62] rather than from Ref. [20] as in the present work). The spread in the N3LO results due to cutoff variations observed here is similar to that reported in Ref. [11] for both $G_C(q)$ and $G_Q(q)$. However, the central values for these observables in the momentum-transfer region $q \gtrsim 2.5$ fm^{-1} reported in that work appear to underestimate the data appreciably. This is not the case here, particularly for $G_Q(q)$, for which the N3LO predictions provide an excellent fit to the measured values (up to $q \simeq 6$ fm^{-1}). These differences likely arise from differences in the deuteron wave functions obtained in Refs. [20,62] (see Fig. 16 in the 2011 review paper [20] for a comparison). Indeed, for these same reasons, the AV18 results are in better agreement with data for $G_C(q)$ in the diffraction region than the N3LO or N3LO* results, while the reverse is true for $G_Q(q)$ at $q \gtrsim 3$ fm^{-1}. The AV18 deuteron wave function, particularly its D-wave component, is markedly different from that of N3LO or N3LO* (see again Fig. 16 in the Machleidt and Entem review [20]).

The individual contributions corresponding to $\Lambda = 500$ MeV and the N3LO potential are listed in Tables VI and VII for q values in the range 0.0–5.1 fm^{-1}. The N2LO (N3LO) charge operators are proportional to $1/m_N^2$ ($1/m_N$), and therefore they vanish in the static limit. The N3LO(OPE) correction is the leading one for $q \gtrsim 1.5$ fm^{-1}, and it is responsible for shifting the zero in the LO $G_C(q)$ to lower q. However, this correction interferes constructively with the LO contribution in the case of $G_Q(q)$. The ν-dependent retardation correction N3LO(ν) is found to be negligible, which allows one to conclude that violations of the unitary equivalence between the OPE potential and associated charge operator is of little numerical import (for $\nu = 0-1$).

The deuteron magnetic moment is one of the two observables utilized to fix the LECs entering the isoscalar current

TABLE VI. Individual contributions to the monopole form factor $G_C(q)$ corresponding to cutoff $\Lambda = 500$ MeV for the N3LO Hamiltonian; $\nu = 1/2$ and $(-x)$ stands for 10^{-x}.

q (fm^{-1})	LO	N2LO	N3LO(OPE)	N3LO(ν)
0.0	1.00	0.00	0.00	0.00
0.3	0.945	−0.340(−3)	−0.211(−3)	−0.600(−6)
0.6	0.792	−0.113(−2)	−0.799(−3)	−0.500(−6)
0.9	0.614	−0.196(−2)	−0.165(−2)	0.530(−5)
1.2	0.452	−0.255(−2)	−0.260(−2)	0.218(−4)
1.5	0.321	−0.280(−2)	−0.349(−2)	0.515(−4)
1.8	0.220	−0.273(−2)	−0.422(−2)	0.932(−4)
2.1	0.146	−0.242(−2)	−0.470(−2)	0.143(−3)
2.4	0.920(−1)	−0.197(−2)	−0.493(−2)	0.195(−3)
2.7	0.547(−1)	−0.145(−2)	−0.493(−2)	0.245(−3)
3.0	0.295(−1)	−0.923(−3)	−0.474(−2)	0.287(−3)
3.3	0.131(−1)	−0.448(−3)	−0.441(−2)	0.319(−3)
3.6	0.295(−2)	−0.518(−4)	−0.400(−2)	0.339(−3)
3.9	−0.278(−2)	0.250(−3)	−0.356(−2)	0.348(−3)
4.2	−0.556(−2)	0.453(−3)	−0.311(−2)	0.346(−3)
4.5	−0.645(−2)	0.566(−3)	−0.269(−2)	0.335(−3)
4.8	−0.621(−2)	0.602(−3)	−0.230(−2)	0.318(−3)
5.1	−0.539(−2)	0.579(−3)	−0.196(−2)	0.297(−3)

TABLE VII. Individual contributions to the quadrupole form factor $G_Q(q)$, normalized at $q = 0$ as in Eq. (3.4), corresponding to cutoff $\Lambda = 500$ MeV for the N3LO Hamiltonian.

q (fm^{-1})	LO	N2LO	N3LO(OPE)	N3LO(ν)
0.0	24.8	−0.172	1.20	−0.108
0.3	23.5	−0.176	1.19	−0.986(−1)
0.6	19.7	−0.182	1.13	−0.968(−1)
0.9	15.3	−0.184	1.04	−0.936(−1)
1.2	11.4	−0.179	0.930	−0.890(−1)
1.5	8.29	−0.167	0.810	−0.829(−1)
1.8	5.92	−0.150	0.690	−0.757(−1)
2.1	4.18	−0.131	0.576	−0.677(−1)
2.4	2.92	−0.111	0.473	−0.596(−1)
2.7	2.03	−0.917(−1)	0.383	−0.515(−1)
3.0	1.39	−0.740(−1)	0.307	−0.440(−1)
3.3	0.947	−0.584(−1)	0.244	−0.371(−1)
3.6	0.635	−0.449(−1)	0.193	−0.310(−1)
3.9	0.418	−0.335(−1)	0.152	−0.257(−1)
4.2	0.268	−0.242(−1)	0.119	−0.212(−1)
4.5	0.167	−0.168(−1)	0.933(−1)	−0.174(−1)
4.8	0.997(−1)	−0.111(−1)	0.731(−1)	−0.142(−1)
5.1	0.568(−1)	−0.686(−2)	0.574(−1)	−0.116(−1)

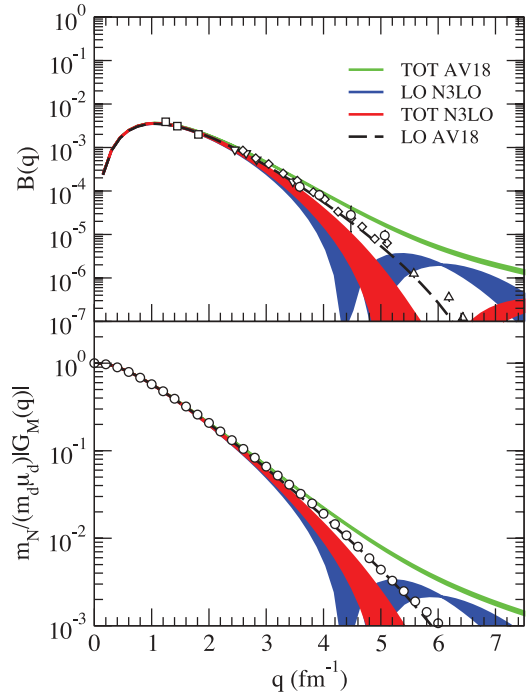

FIG. 5. (Color online) The deuteron $B(q)$ structure function (top panel) and magnetic form factor $G_M(q)$ (bottom panel), obtained at leading order (LO) and with inclusion of current operators up to N3LO (TOT), compared with the experimental data from Refs. [36,42,43,58–60]. Predictions corresponding to cutoffs Λ in the range 500–600 MeV are displayed by the bands.

operators at N3LO, denoted as N3LO(nm) and N3LO(OPE) in Sec. IV A and Table II. The structure function $B(q)$ and magnetic form factor $G_M(q)$, obtained with the AV18 and chiral potentials and currents at LO and by including corrections up to N3LO, are compared to data in Fig. 5. There is generally good agreement between theory and experiment for q values up to $\simeq 2$ fm^{-1}. At higher q values, the results corresponding to the chiral (AV18) potential underpredict (overpredict) the data significantly when the current includes up to N3LO corrections. In particular, the diffraction seen in the data at $q \simeq 6.5$ fm^{-1} is absent in the AV18 calculations and is shifted to lower q values in the N3LO or N3LO* ones. There are large differences between the N3LO or N3LO* and AV18 results with the LO current, which simply reflect differences in the S- and D-wave components of the deuteron wave functions corresponding to these potentials. The cutoff dependence is large for the chiral potentials, while it remains quite modest for the AV18 potential over the whole momentum transfer range. This is consistent with the rather different sensitivity of the LECs d_1^S and d_2^S to variations of Λ in the 500–600 MeV range obtained with either the chiral potential or AV18 (see Table I). There is a mismatch in the chiral counting between the potentials of Ref. [20] at order Q^4 and the present current at order eQ. This becomes obvious when considering current conservation, which for these potentials would require accounting for terms up to order eQ^3 in the current, well beyond available derivations [5,7,8] at this time.

The AV18 results obtained here for $B(q)$ are similar to those reported in the conventional framework of Ref. [23] (see curve labeled IA + $\rho\pi\gamma$-NR in Fig. 5). In that work, the current included the standard impulse-approximation (IA) term—the LO current in χEFT—and the two-body term from $\rho\pi\gamma$ transitions. The size, and in fact sign, of the $\rho\pi\gamma$ contribution were found to depend on whether the current was derived by retaining the fully relativistic (R) structure of the associated Feynman amplitude or only the leading-order term in its nonrelativistic (NR) expansion—in this latter case, it is essentially the N3LO(OPE) current of Eq. (2.24). Indeed, the $\rho\pi\gamma$ contribution had the same (opposite) sign as the IA when it was evaluated with the NR (R) current, and the IA + $\rho\pi\gamma$(NR) results overestimated the data by an amount similar to that shown in Fig. 5.

Recently, a calculation of the deuteron magnetic structure, based on the same χEFT utilized here, has appeared in the literature [12]. It uses chiral potentials at order Q^2 derived in Ref. [62] and a different strategy from that adopted here for constraining the two LECs in the isoscalar N3LO current. One of them is still fixed by reproducing μ_d; the other, however, is determined by a fit to $B(q)$ data up to $q \simeq 2$ fm^{-1}. Predictions for this observable in $q = 2$–4 fm^{-1} seem to overestimate the data at the highest q values ($q \gtrsim 3.5$ fm^{-1}), but they display much less cutoff dependence than obtained here. This is clearly due to the different way in which the LECs are constrained in the two calculations.

Finally, in Table VIII we list the individual contributions to $G_M(q)$ obtained with the N3LO potential and cutoff $\Lambda = 500$ MeV. The notation is as follows: LO is the leading-order (eQ^{-2}) current of Eq. (2.4); N2LO is the relativistic correction of order $n = 0$ (eQ^0) in Eq. (2.10); and N3LO(min), N3LO(nm), and N3LO(OPE) are the corrections of order $n = 1$ (eQ) in Eqs. (2.20), (2.21), and (2.24), respectively. The N3LO(min) and N3LO(nm) contributions from the minimal

TABLE VIII. Individual contributions to the magnetic form factor $G_M(q)$, normalized at $q = 0$ as in Eq. (3.4), corresponding to cutoff $\Lambda = 500$ MeV for the N3LO Hamiltonian; $(-x)$ stands for 10^{-x}.

q (fm^{-1})	LO	N2LO	N3LO(min)	N3LO(nm)	N3LO(OPE)
0.0	1.71	−0.144(−1)	0.508(−1)	−0.353(−1)	0.483(−2)
0.3	1.62	−0.150(−1)	0.508(−1)	−0.353(−1)	0.480(−2)
0.6	1.36	−0.159(−1)	0.495(−1)	−0.343(−1)	0.473(−2)
0.9	1.07	−0.166(−1)	0.474(−1)	−0.329(−1)	0.461(−2)
1.2	0.807	−0.166(−1)	0.447(−1)	−0.310(−1)	0.444(−2)
1.5	0.590	−0.159(−1)	0.416(−1)	−0.289(−1)	0.423(−2)
1.8	0.422	−0.144(−1)	0.382(−1)	−0.265(−1)	0.399(−2)
2.1	0.296	−0.125(−1)	0.347(−1)	−0.241(−1)	0.372(−2)
2.4	0.202	−0.104(−1)	0.312(−1)	−0.217(−1)	0.344(−2)
2.7	0.134	−0.818(−2)	0.279(−1)	−0.194(−1)	0.315(−2)
3.0	0.860(−1)	−0.608(−2)	0.248(−1)	−0.172(−1)	0.286(−2)
3.3	0.522(−1)	−0.418(−2)	0.219(−1)	−0.152(−1)	0.258(−2)
3.6	0.291(−1)	−0.254(−2)	0.193(−1)	−0.134(−1)	0.231(−2)
3.9	0.138(−1)	−0.120(−2)	0.169(−1)	−0.117(−1)	0.206(−2)
4.2	0.415(−2)	−0.159(−3)	0.148(−1)	−0.103(−1)	0.183(−2)
4.5	−0.152(−2)	0.581(−3)	0.130(−1)	−0.899(−2)	0.162(−2)
4.8	−0.444(−2)	0.105(−2)	0.113(−1)	−0.785(−2)	0.143(−2)
5.1	−0.554(−2)	0.128(−2)	0.988(−2)	−0.686(−2)	0.126(−2)

and nonminimal contact currents cancel to a large extent, and their combined effect is comparable to the N3LO(OPE) contribution. This interplay among different corrections, however, depends strongly on Λ and the Hamiltonian model considered.

C. Static properties and form factors of the trinucleons

The notation for the various components of the charge operator is the same as given at the beginning of Sec. IV B, except that now the one-loop (isovector) corrections at N4LO contribute too, since the ^{3}He and ^{3}H nuclei have predominantly total isospin $T = 1/2$. As a matter of fact, the hyperspherical harmonics wave functions utilized to represent their ground states also include small $T = 3/2$ admixtures due to isospin-symmetry-breaking terms induced by the electromagnetic and strong interactions.

There are no unknown LECs entering the charge operator up to N4LO, and the predicted root-mean-square charge radii of ^{3}He and ^{3}H, obtained with the N3LO/N2LO and AV18/UIX combinations of two- and three-nucleon potentials and cutoffs in the 500–600 MeV range, are listed in Table IX. Corrections at N2LO, N3LO, and N4LO are negligible—the corresponding operators vanish at $q = 0$. The spread between the N3LO/N2LO ($\Lambda = 500$ MeV) and N3LO*/N2LO* ($\Lambda = 600$ MeV) results at LO is about 0.5%, which is much smaller, particularly for ^{3}H, than the experimental error. The predicted radii for both Hamiltonian models are within 0.5% of the current experimental central values.

The calculated charge form factors of ^{3}He and ^{3}H, and their isoscalar and isovector combinations $F_C^S(q)$ and $F_C^V(q)$, normalized, respectively, to 3/2 and 1/2 at $q = 0$, are compared to data in Fig. 6. The agreement between theory and experiment is excellent for $q \lesssim 2.5$ fm^{-1}. At larger values of the momentum transfer, there is a significant sensitivity to cutoff variations in the results obtained with the chiral potentials. This cutoff dependence is large at LO and is reduced, at least in ^{3}He, when corrections up to N4LO are included. These corrections have sign opposite to that at LO and tend to shift the zeros in the form factors to lower momentum transfers, bringing theory closer to experiment in the diffraction region.

As already remarked, the chiral (and conventional) two-nucleon potentials utilized in the present study ignore retardation corrections in their OPE and TPE components, which corresponds to the choice $\nu = 1/2$ in the nonstatic pieces of the corresponding potentials and accompanying charge operators in Eqs. (2.13) and (2.37) [6]. Figure 7 is meant to illustrate how inconsistencies between the potential and charge operator impact predictions for the ^{3}H form factor, by presenting results obtained with the N3LO/N2LO Hamiltonian ($\nu = 1/2$), cutoff $\Lambda = 500$ MeV, and N3LO and N4LO corrections with $\nu = 0$ and 1 in the charge operator. Their effect is negligible.

In Fig. 8, we show cumulatively the LO, N2LO, N3LO, and N4LO contributions to the charge form factors of ^{3}He and ^{3}H. The N2LO contributions are smallest, while the N3LO

TABLE IX. Cumulative contributions in femtometers to the ^{3}He and ^{3}H root-mean-square charge radii corresponding to $\nu = 1/2$ and cutoffs $\Lambda = 500$ and 600 MeV, obtained with the N3LO/N2LO and N3LO*/N2LO* Hamiltonians; results in parentheses are relative to the AV18/UIX Hamiltonian. The experimental values for the ^{3}He and ^{3}H charge radii are [60] 1.959 ± 0.030 and 1.755 ± 0.086 fm, respectively.

Λ	^{3}He		^{3}H	
	500	600	500	600
LO	1.966(1.950)	1.958(1.950)	1.762(1.743)	1.750(1.743)
N2LO	1.966(1.950)	1.958(1.950)	1.762(1.743)	1.750(1.743)
N3LO	1.966(1.950)	1.958(1.950)	1.762(1.743)	1.750(1.743)
N4LO	1.966(1.950)	1.958(1.950)	1.762(1.743)	1.750(1.743)

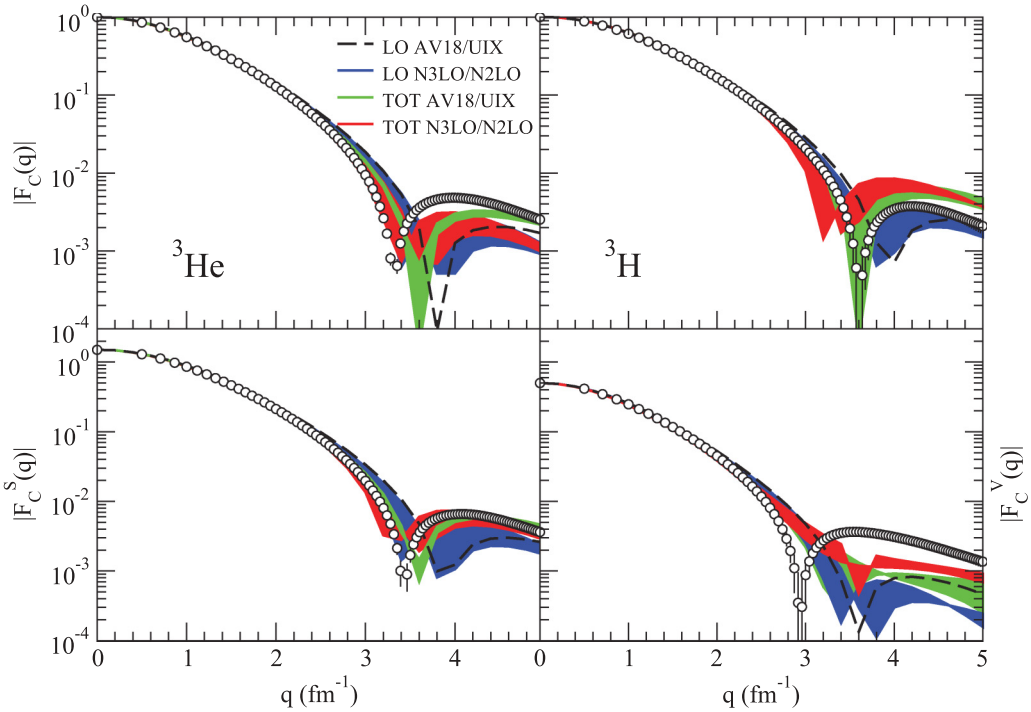

FIG. 6. (Color online) The ^{3}He and ^{3}H charge form factors (top panels) and their isoscalar and isovector combinations (bottom panels), obtained at leading order (LO) and with inclusion of charge operators up to N4LO (TOT), compared with experimental data [61]. Predictions corresponding to $\nu = 1/2$ and cutoffs Λ in the range 500–600 MeV are displayed by the bands.

and N4LO ones turn out to be comparable. This is illustrated explicitly in Tables X and XI, where we list the individual contributions of the various terms entering at each order. In these tables, we denote with N3LO(OPE) and N3LO(ν) the operators in Eqs. (2.12) and in Eqs. (2.13) and (2.14), respectively, and we denote with N4LO(cd), N4LO(ef; ν), and N4LO(ij) those in Eqs. (2.35) and (2.36), Eqs. (2.37) and (2.38), and Eqs. (2.39) and (2.40). Among the corrections at N3LO the OPE term—column N3LO(OPE)—illustrated by panel (a) in Fig. 1 is dominant, while among those at N4LO the TPE terms—columns N4LO(ef; ν) and N4LO(ij)—illustrated by panels (e) and (f) and (i) and (j) in Fig. 3 are dominant. The N3LO(OPE) and N4LO(ef; ν) and N4LO(ij) contributions are of similar magnitude; indeed there is no hint of suppression in going from N3LO to N4LO, as one would have naively expected on the basis of power counting.

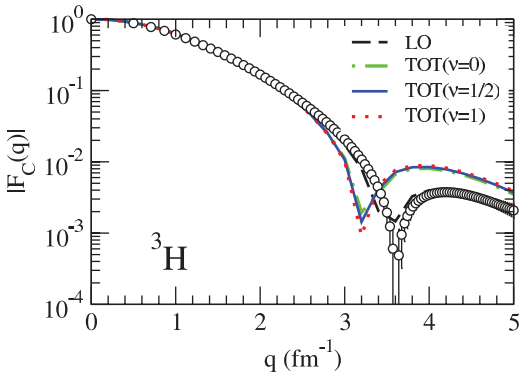

FIG. 7. (Color online) The ^{3}H charge form factor obtained with the N3LO/N2LO Hamiltonian, cutoff $\Lambda = 500$ MeV, and charge operators up to N4LO corresponding to $\nu = 0$, $1/2$, and 1.

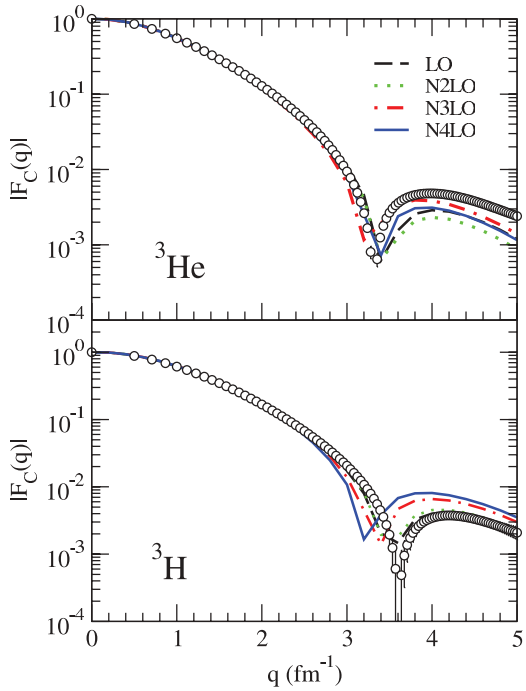

FIG. 8. (Color online) Cumulative contributions to the ^{3}He and ^{3}H charge form factors, obtained with the N3LO/N2LO Hamiltonian, cutoff $\Lambda = 500$ MeV, and $\nu = 1/2$, from the components of the charge operator order by order.

TABLE X. Individual contributions to the ^{3}He charge form factor, obtained with the N3LO/N2LO Hamiltonian, cutoff $\Lambda = 500$ MeV, and $\nu = 1/2$; $(-x)$ stands for 10^{-x}.

q (fm^{-1})	LO	N2LO	N3LO(OPE)	N3LO(ν)	N4LO(cd)	N4LO(ef; ν)	N4LO(ij)
0.0	1.00	0.00	0.00	0.00	0.00	0.00	0.00
0.2	0.983	−0.561(−3)	−0.152(−3)	0.100(−4)	−0.477(−5)	0.904(−4)	0.301(−4)
0.6	0.807	−0.406(−2)	−0.125(−2)	0.870(−4)	0.108(−3)	0.785(−4)	0.346(−3)
1.0	0.562	−0.760(−2)	−0.289(−2)	0.205(−3)	0.296(−3)	0.126(−4)	0.835(−3)
1.4	0.342	−0.876(−2)	−0.434(−2)	0.324(−3)	0.503(−3)	−0.134(−3)	0.132(−2)
1.8	0.185	−0.758(−2)	−0.513(−2)	0.409(−3)	0.680(−3)	−0.347(−3)	0.167(−2)
2.2	0.892(−1)	−0.525(−2)	−0.516(−2)	0.447(−3)	0.796(−3)	−0.585(−3)	0.184(−2)
2.6	0.366(−1)	−0.288(−2)	−0.463(−2)	0.433(−3)	0.841(−3)	−0.796(−3)	0.184(−2)
3.0	0.111(−1)	−0.107(−2)	−0.380(−2)	0.385(−3)	0.821(−3)	−0.938(−3)	0.170(−2)
3.4	0.623(−3)	−0.969(−5)	−0.292(−2)	0.315(−3)	0.750(−3)	−0.989(−3)	0.148(−2)
3.8	−0.258(−2)	0.488(−3)	−0.213(−2)	0.241(−3)	0.644(−3)	−0.949(−3)	0.122(−2)
4.2	−0.276(−2)	0.577(−3)	−0.148(−2)	0.174(−3)	0.522(−3)	−0.831(−3)	0.957(−3)
4.6	−0.200(−2)	0.476(−3)	−0.994(−3)	0.117(−3)	0.395(−3)	−0.660(−3)	0.702(−3)
5.0	−0.119(−2)	0.318(−3)	−0.642(−3)	0.730(−4)	0.274(−3)	−0.469(−3)	0.476(−3)

The ^{3}He contributions in Table X have been divided by the number of protons $Z = 2$ in order to have the form factor normalized to one at $q = 0$. The N4LO charge operators are isovector and, if ^{3}He and ^{3}H were pure $T = 1/2$ states, then $2 \times \text{N4LO}(^3\text{He}) = -\text{N4LO}(^3\text{H})$. That this equality is not exactly satisfied reflects the fact that the present ^{3}He and ^{3}H wave functions are not simply the charge mirror of each other—that is, $(\prod_i \tau_{i,x})|^3\text{He}\rangle \neq |^3\text{H}\rangle$, where $\tau_{i,x}$ is the x component of nucleon i isospin operator.

Moving on to the magnetic structure of the trinucleons, we note that the isoscalar combination μ_S of ^{3}He and ^{3}H magnetic moments is used to fix one of the two (isoscalar) LECs entering the current at N3LO. Both the isovector combination μ_V and the np radiative capture cross section σ_{np} are used to fix the isovector LECs in set I of the N3LO currents, while in sets II and III one of these LECs is fixed by Δ dominance, and the other is determined by reproducing σ_{np} (μ_V) in set II (III) (see Tables II and IV). By construction, then, the ^{3}He and ^{3}H magnetic moments are exactly reproduced in sets I and III, while in set II they are calculated to be, respectively, -2.186 $(-2.196)\mu_N$ and 3.038 $(3.048)\mu_N$ with the N3LO/N2LO (N3LO*/N2LO*) Hamiltonian and $\Lambda = 500$ (600) MeV, and similar results are obtained with the AV18/UIX Hamiltonian. These should be compared to the experimental values of $-2.127\mu_N$ and $2.979\mu_N$.

The ^{3}He and ^{3}H magnetic radii corresponding to sets I–III are given in Table XII. The predicted values are consistent with experiment, although the measurements have rather large errors (10% for ^{3}H). Their spread as Λ varies in the 500–600 MeV range is at the 1% level or less. A recent quantum Monte Carlo study [63], using wave functions derived from conventional two- and three-nucleon potentials (the AV18 and Illinois 7 model [64]) and set III of χEFT currents, has led to predictions for magnetic moments and transitions in nuclei with $A \leqslant 9$ in excellent agreement with the measured values. Therefore in the following, unless stated otherwise, we adopt

TABLE XI. Individual contributions to the ^{3}H charge form factor, obtained with the N3LO/N2LO Hamiltonian, cutoff $\Lambda = 500$ MeV, and $\nu = 1/2$; $(-x)$ stands for 10^{-x}.

q (fm^{-1})	LO	N2LO	N3LO(OPE)	N3LO(ν)	N4LO(cd)	N4LO(ef; ν)	N4LO(ij)
0.0	1.00	0.00	0.00	0.00	0.00	0.00	0.00
0.2	0.991	0.647(−3)	−0.185(−3)	0.110(−4)	0.103(−4)	−0.190(−3)	−0.633(−4)
0.6	0.844	0.462(−2)	−0.152(−2)	0.880(−4)	−0.229(−3)	−0.136(−3)	−0.729(−3)
1.0	0.621	0.844(−2)	−0.356(−2)	0.245(−3)	−0.628(−3)	0.459(−4)	−0.176(−2)
1.4	0.402	0.940(−2)	−0.543(−2)	0.462(−3)	−0.107(−2)	0.396(−3)	−0.278(−2)
1.8	0.231	0.784(−2)	−0.653(−2)	0.686(−3)	−0.144(−2)	0.874(−3)	−0.352(−2)
2.2	0.118	0.520(−2)	−0.671(−2)	0.858(−3)	−0.169(−2)	0.138(−2)	−0.389(−2)
2.6	0.517(−1)	0.270(−2)	−0.615(−2)	0.944(−3)	−0.179(−2)	0.182(−2)	−0.389(−2)
3.0	0.174(−1)	0.903(−3)	−0.519(−2)	0.940(−3)	−0.174(−2)	0.210(−2)	−0.361(−2)
3.4	0.204(−2)	−0.972(−4)	−0.411(−2)	0.867(−3)	−0.159(−2)	0.218(−2)	−0.314(−2)
3.8	−0.328(−2)	−0.483(−3)	−0.310(−2)	0.615(−3)	−0.136(−2)	0.206(−2)	−0.259(−2)
4.2	−0.403(−2)	−0.508(−3)	−0.225(−2)	0.543(−3)	−0.110(−2)	0.178(−2)	−0.201(−2)
4.6	−0.313(−2)	−0.383(−3)	−0.159(−2)	0.483(−3)	−0.825(−3)	0.139(−2)	−0.147(−2)
5.0	−0.196(−2)	−0.232(−3)	−0.108(−2)	0.364(−3)	−0.565(−3)	0.942(−3)	−0.985(−3)

TABLE XII. Cumulative contributions in femtometers to the ^{3}He and ^{3}H root-mean-square magnetic radii corresponding to cutoffs $\Lambda = 500$ and 600 MeV, obtained with the N3LO/N2LO and N3LO*/N2LO* Hamiltonians; results in parentheses are relative to the AV18/UIX Hamiltonian. Predictions corresponding to sets I, II, and II of isovector LECs d_1^V and d_2^V in Table III are listed. The experimental values for the ^{3}He and ^{3}H magnetic radii are [60] 1.965 ± 0.153 and 1.840 ± 0.181 fm, respectively.

Λ	^{3}He		^{3}H	
	500	600	500	600
LO	2.098(2.092)	2.090(2.092)	1.924(1.918)	1.914(1.918)
NLO	1.990(1.981)	1.983(1.974)	1.854(1.847)	1.845(1.841)
N2LO	1.998(1.992)	1.989(1.984)	1.865(1.859)	1.855(1.854)
N3LO(I)	1.924(1.931)	1.910(1.972)	1.808(1.800)	1.796(1.819)
N3LO(II)	1.901(1.890)	1.883(1.896)	1.789(1.774)	1.773(1.778)
N3LO(III)	1.927(1.915)	1.913(1.924)	1.808(1.792)	1.794(1.797)

set III of isovector LECs. We disregard set I for the reasons already explained in Sec. IV A.

The magnetic form factors of ^{3}He and ^{3}H and their isoscalar and isovector combinations $F_M^S(q)$ and $F_M^V(q)$, normalized, respectively, as μ_S and μ_V at $q = 0$, at LO and with inclusion of corrections up to N3LO in the current, are displayed in Fig. 9. As is well known from studies based on the conventional meson-exchange framework (see the review [16] and references therein), two-body currents are crucial for "filling in" the zeros obtained in the LO calculation due to the interference between the S- and D-state components in the ground states of these nuclei. For $q \lesssim 2$ fm^{-1} there is excellent agreement between the present χEFT predictions and experiment. However, as the momentum transfer increases, even after making allowance for the significant cutoff dependence, theory tends to underestimate the data; in particular it predicts the zeros in both form factors occurring at significantly lower values of q than observed. Thus, the first diffraction region remains problematic for the present theory, confirming earlier conclusions derived from studies in the conventional framework [65,66].

Figure 10 illustrates the sensitivity of the N3LO predictions on the different ways in which the isovector LECs are constrained in sets I, II, and III. The set I results are strongly at variance with data. Set II leads to two-body current contributions larger than in set III and consequently, in contrast to set III, the corresponding form factors reproduce the data in the diffraction region. However, the cutoff variation of the results is considerably larger than for set III, as reflected in the change of the LEC d_1^V for $\Lambda = 500$–600 MeV in Table III. Furthermore, set II overestimates μ_V by about 3%.

Figure 11 exhibits cumulatively the LO, NLO, N2LO, and N3LO contributions to the ^{3}He and ^{3}H magnetic form factors, obtained with the N3LO/N2LO Hamiltonian and cutoff $\Lambda = 500$ MeV. Tables XIII and XIV list the individual components of these contributions at selected values of q. The notation is as follows: with LO we denote the one-body current in Eq. (2.4), with NLO the OPE currents in Eq. (2.7), with N2LO the relativistic correction to the one-body current in Eq. (2.10),

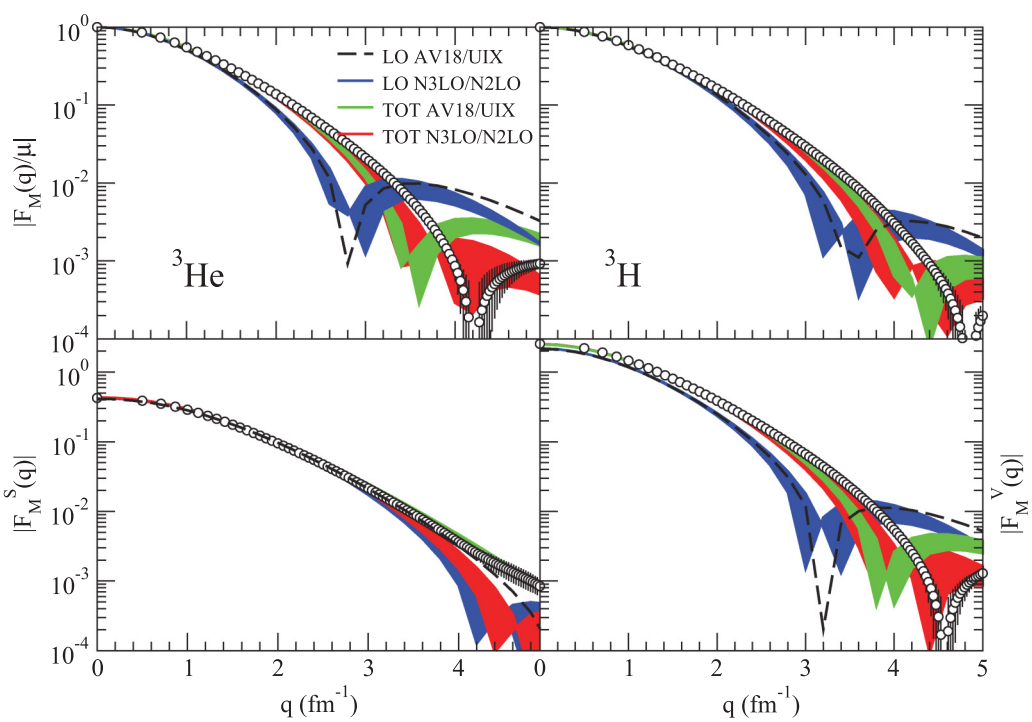

FIG. 9. (Color online) The ^{3}He and ^{3}H magnetic form factors (top panels) and their isoscalar and isovector combinations (bottom panels), obtained at leading order (LO) and with inclusion of current operators up to N3LO (TOT) corresponding to the LEC's d_1^S and d_2^S in Table I and to set III of isovector LEC's d_1^V and d_2^V in Table III, compared with experimental data [61]. Predictions relative to cutoffs Λ in the range 500–600 MeV are displayed by the bands.

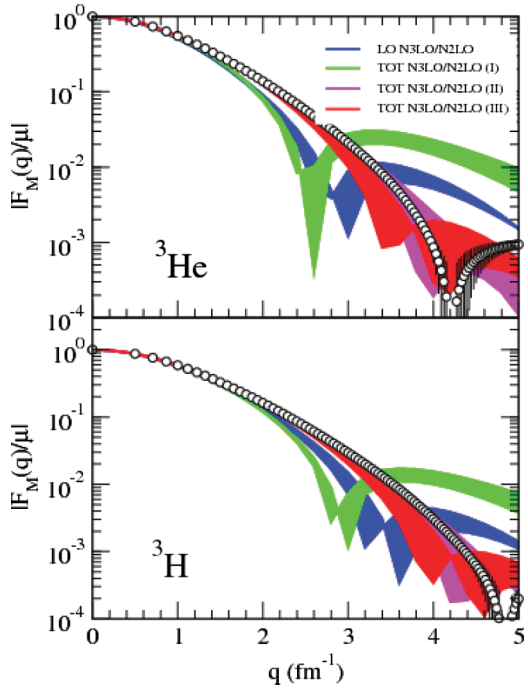

FIG. 10. (Color online) The ^{3}He and ^{3}H magnetic form factors, obtained at leading order (LO) and with inclusion of current operators up to N3LO (TOT) corresponding to sets I, II, and III of isovector LECs d_1^V and d_2^V in Table III, compared with experimental data [61]. Predictions, relative to the N3LO/N2LO Hamiltonian and corresponding to cutoffs $\Lambda = 500$–600 MeV, are displayed by the bands.

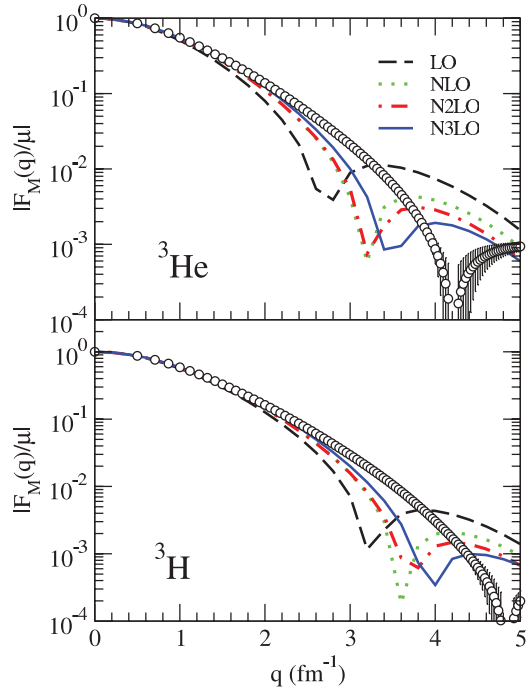

FIG. 11. (Color online) Cumulative contributions to the ^{3}He and ^{3}H magnetic form factors, obtained with the N3LO/N2LO Hamiltonian and cutoff $\Lambda = 500$ MeV, from the components of the current operator order by order. Set III is adopted for the isovector LECs d_1^V and d_2^V in Table III.

with N3LO(loop) the one-loop current in Eq. (2.29); with N3LO(min) the "minimal" contact current in Eq. (2.20), with N3LO(nm) the "nonminimal" contact current in Eq. (2.21), and finally with N3LO(OPE) the OPE currents at N3LO given in Eqs. (2.22) and (2.24). The NLO and N3LO(loop) are purely isovector, while the remaining operators have both isoscalar and isovector terms. As in the case of the charge form factors, the expected suppression of the NnLO corrections as $(q/\Lambda_\chi)^n$, where we have taken $Q \sim q$ as the "low-momentum" scale and $\Lambda_\chi = 700$–800 MeV as the chiral-symmetry-breaking scale, does not appear to be satisfied (not even at the smallest q values).

V. CONCLUSIONS

In the first part of this study (Sec. II and Appendices A and B), we have clarified the origin of some of the differences in the N3LO and N4LO corrections to the current and charge operators, reported in Refs. [5,6,8]. In contrast to the authors of Ref. [8], we have not yet provided a complete

TABLE XIII. Individual contributions to the ^{3}He magnetic form factor, obtained with the N3LO/N2LO Hamiltonian, cutoff $\Lambda = 500$ MeV, and set III of isovector LECs; $(-x)$ stands for 10^{-x}.

q (fm^{-1})	LO	NLO	N2LO	N3LO(L)	N3LO(min)	N3LO(nm)	N3LO(OPE)
0.2	−1.72	−0.196	0.162(−1)	−0.385(−1)	0.511(−1)	−0.109	−0.488(−1)
0.6	−1.37	−0.184	0.160(−1)	−0.358(−1)	0.478(−1)	−0.101	−0.414(−1)
1.0	−0.898	−0.160	0.142(−1)	−0.310(−1)	0.421(−1)	−0.877(−1)	−0.293(−1)
1.4	−0.495	−0.128	0.105(−1)	−0.253(−1)	0.352(−1)	−0.716(−1)	−0.164(−1)
1.8	−0.228	−0.934(−1)	0.595(−2)	−0.196(−1)	0.280(−1)	−0.554(−1)	−0.584(−2)
2.2	−0.794(−1)	−0.632(−1)	0.189(−2)	−0.145(−1)	0.214(−1)	−0.410(−1)	0.106(−2)
2.6	−0.964(−2)	−0.402(−1)	−0.912(−3)	−0.103(−1)	0.159(−1)	−0.292(−1)	0.448(−2)
3.0	0.158(−1)	−0.241(−1)	−0.234(−2)	−0.709(−2)	0.114(−1)	−0.201(−1)	0.542(−2)
3.4	0.199(−1)	−0.138(−1)	−0.266(−2)	−0.473(−2)	0.796(−2)	−0.134(−1)	0.496(−2)
3.8	0.159(−1)	−0.756(−2)	−0.231(−2)	−0.306(−2)	0.543(−2)	−0.869(−2)	0.392(−2)
4.2	0.103(−1)	−0.396(−2)	−0.170(−2)	−0.191(−2)	0.360(−2)	−0.543(−2)	0.281(−2)
4.6	0.576(−2)	−0.198(−2)	−0.108(−2)	−0.115(−3)	0.231(−2)	−0.326(−2)	0.185(−2)
5.0	0.272(−2)	−0.929(−3)	−0.584(−3)	−0.658(−3)	0.143(−2)	−0.186(−2)	0.113(−2)

TABLE XIV. Individual contributions to the ^{3}H magnetic form factor, obtained with the N3LO/N2LO Hamiltonian, cutoff $\Lambda = 500$ MeV, and set III of isovector LECs; $(-x)$ stands for 10^{-x}.

q (fm^{-1})	LO	NLO	N2LO	N3LO(L)	N3LO(min)	N3LO(nm)	N3LO(OPE)
0.2	2.56	0.199	−0.325(−1)	0.413(−1)	0.178(−1)	0.659(−1)	0.517(−1)
0.6	2.11	0.188	−0.319(−1)	0.380(−1)	0.163(−1)	0.612(−1)	0.439(−1)
1.0	1.47	0.164	−0.290(−1)	0.333(−1)	0.138(−1)	0.530(−1)	0.312(−1)
1.4	0.894	0.131	−0.232(−1)	0.272(−1)	0.107(−1)	0.432(−1)	0.176(−1)
1.8	0.477	0.964(−1)	−0.159(−1)	0.211(−1)	0.763(−2)	0.334(−1)	0.627(−2)
2.2	0.221	0.656(−1)	−0.894(−2)	0.156(−1)	0.502(−2)	0.247(−1)	−0.119(−2)
2.6	0.834(−1)	0.418(−1)	−0.354(−2)	0.111(−1)	0.299(−2)	0.176(−1)	−0.450(−2)
3.0	0.188(−1)	0.252(−1)	0.117(−3)	0.764(−2)	0.155(−2)	0.122(−1)	−0.615(−2)
3.4	−0.591(−2)	0.145(−1)	0.156(−2)	0.508(−2)	0.607(−3)	0.815(−2)	−0.576(−2)
3.8	−0.117(−1)	0.796(−2)	0.201(−2)	0.327(−2)	0.353(−4)	0.531(−2)	−0.469(−2)
4.2	−0.101(−1)	0.419(−2)	0.177(−2)	0.203(−2)	−0.275(−3)	0.337(−2)	−0.350(−2)
4.6	−0.666(−2)	0.210(−2)	0.128(−2)	0.121(−2)	−0.415(−3)	0.207(−2)	−0.243(−2)
5.0	−0.365(−2)	0.993(−3)	0.777(−3)	0.681(−3)	−0.451(−3)	0.124(−2)	−0.159(−2)

derivation of the contributions associated with loop corrections to tree-level (OPE) current and charge operators (although some were discussed in Ref. [5]); in particular, we have not carried out a full-fledged renormalization of these operators in our formalism. However, as pointed out in Sec. II A, the renormalized OPE current in Eq. (4.28) of Ref. [8] leads to the same magnetic moment operator obtained from the currents in Eqs. (2.7), (2.22), and (2.24) of the present work, with the understanding, of course, that the LECs entering these equations are assumed to have been renormalized. There remain differences in the pion-loop corrections to the short-range charge operator, Eq. (5.5) of Ref. [8] and Eqs. (2.39) and (2.40), the latter presumably due to the different ways in which noniterative pieces of reducible contributions are isolated in the two formalisms. The authors of Refs. [7,8] use TOPT in combination with the unitary transformation method [67] to decouple, in the Hilbert space of pions and nucleons, the states consisting of nucleons only from those including, in addition, pions. In contrast, we construct a potential such that, when iterated in the Lippmann-Schwinger equation, leads to a T-matrix matching, order by order in the power counting, the χEFT amplitude calculated in TOPT [6,68].

In the second part of this study, we have provided predictions for the static properties, including charge and magnetic radii and magnetic moments, and elastic form factors of the deuteron and trinucleons. The wave functions describing these nuclei were derived from either χEFT or conventional two- and three-nucleon potentials. The matrix elements of the χEFT charge and current operators were evaluated in momentum space with Monte Carlo methods.

The χEFT calculations (based on the N3LO potential) and the hybrid ones (based on AV18) reproduce very well the observed electromagnetic structure of the deuteron for momentum transfers q up to 2–3 fm^{-1}. In some cases, as in the $A(q)$ structure function, the agreement between the experimental and χEFT calculated values extends up to $q \lesssim 6$ fm^{-1}, a much higher momentum transfer than one would naively expect the present expansion to be valid for. On the other hand, the measured $B(q)$ structure function is significantly underpredicted (overpredicted) for $q \gtrsim 3$ fm^{-1} in the χEFT (hybrid) calculations. The χEFT results, in contrast to the hybrid ones, have a rather large cutoff dependence. This cutoff dependence originates, in the hybrid calculations, solely from that in the N3LO current, while in the χEFT calculation it also reflects the Λ dependence intrinsic to the potential (the N3LO potential for $\Lambda = 500$ MeV or the N3LO* potential for $\Lambda = 600$ MeV).

The calculated ^{3}He and ^{3}H charge form factors are in excellent agreement with data up to $q \lesssim 3$ fm^{-1}. However, the observed positions of the zeros are not generally well reproduced by theory, and the measured ^{3}He (^{3}H) form factor in the region of the secondary maximum at $q \simeq 4$ fm^{-1} is underestimated (overestimated) in both χEFT and hybrid calculations. A glance at the $F_C^S(q)$ and $F_C^V(q)$ values in Fig. 6 suggests that two-body isovector contributions to the charge operator should be considerably larger (in magnitude) than presently calculated, in order to shift the zero in $F_C^V(q)$ to smaller q.

The isovector currents at N3LO depend on two LECs (d_1^V and d_2^V), which have been fixed in one of three different ways: by reproducing the experimental np radiative capture cross section σ_{np} and isovector magnetic moment μ_V of the trinucleons simultaneously (set I) or by using Δ dominance to constrain d_2^V and by determining d_1^V so as to fit either σ_{np} (set II) or μ_V (set III). Set I is not seriously considered for the reasons explained in Sec. IV A. The ^{3}He and ^{3}H magnetic form factors calculated with N3LO currents corresponding to set III, while in excellent agreement with data for $q \lesssim 3$ fm^{-1}, underpredict them at higher momentum transfers. On the other hand, set II N3LO currents in the χEFT calculations (based on the N3LO/N2LO and N3LO*/N2LO* Hamiltonians) would lead to significantly better agreement with data over the whole range of momentum transfers (see Fig. 10), but they would overestimate the observed μ_V by $\simeq$3%.

ACKNOWLEDGMENTS

R.S. would like to thank the T-2 group in the Theoretical Division at Los Alamos National Laboratory, and especially J. Carlson and S. Gandolfi, for the support and warm hospitality

extended to him during a sabbatical visit in the Fall 2012, during which part of this work was completed. The work of R.S. is supported by the US Department of Energy, Office of Nuclear Physics, under Contract No. DE-AC05-06OR23177. The calculations were made possible by grants of computing time from the National Energy Research Scientific Computing Center.

APPENDIX A: MINIMAL CONTACT CURRENTS

In this Appendix, we show the equivalence between the minimal contact current in Eq. (3.11) of Ref. [5] and that given in Eq. (2.20) in terms of the known low-energy constants $C_1, \ldots, C_7$. One way to achieve this is to start from the Lagrangian given in Eq. (2.13) of Ref. [69] (where additional terms with fixed coefficients proportional to $1/m_N^2$ have been ignored),

$$\begin{aligned}\mathcal{L} = &-\tfrac{1}{2}C_S\, O_S - \tfrac{1}{2}C_T\, O_T - \tfrac{1}{2}C_1(O_1 + 2\,O_2)\\ &+ \tfrac{1}{8}C_2(2\,O_2 + O_3) - \tfrac{1}{2}C_3(O_9 + 2\,O_{12})\\ &- \tfrac{1}{8}C_4(O_9 + O_{14}) + \tfrac{1}{4}C_5(O_6 - O_5)\\ &- \tfrac{1}{2}C_6(O_7 + 2\,O_{10}) - \tfrac{1}{16}C_7(O_7 + O_8 + 2\,O_{13}),\end{aligned} \tag{A1}$$

where the operators O_i are the standard set in Table I of Ref. [69], and then to gauge the gradients as $\nabla N \to \nabla N - i\,e\,e_N\,\mathbf{A}\,N$ to obtain

$$\begin{aligned}\mathbf{j}^{(1)}_{\mathrm{a,min}} = &\frac{C_2}{4}(\tau_{1,z} - \tau_{2,z})(\mathbf{K}_1 - \mathbf{K}_2)\\ &+ \frac{C_4}{4}(\tau_{1,z} - \tau_{2,z})\,\boldsymbol{\sigma}_1\cdot\boldsymbol{\sigma}_2\,(\mathbf{K}_1 - \mathbf{K}_2)\\ &- \frac{i\,C_5}{4}\,(\boldsymbol{\sigma}_1 + \boldsymbol{\sigma}_2)\times(e_1\,\mathbf{k}_1 + e_2\,\mathbf{k}_2)\\ &+ \frac{C_7}{8}(\tau_{1,z} - \tau_{2,z})\,[\boldsymbol{\sigma}_1\cdot(\mathbf{K}_1 - \mathbf{K}_2)\,\boldsymbol{\sigma}_2\\ &+ \boldsymbol{\sigma}_2\cdot(\mathbf{K}_1 - \mathbf{K}_2)\,\boldsymbol{\sigma}_1].\end{aligned} \tag{A2}$$

Because of the antisymmetry of two-nucleon states, we have

$$\mathbf{j}^{(1)}_{\mathrm{a,min}} = -P^{\tau}\,P^{\sigma}\,P^{\mathrm{space}}\,\mathbf{j}^{(1)}_{\mathrm{a,min}}, \tag{A3}$$

where P^{space}, P^{σ}, and P^{τ} are, respectively, the space, spin, and isospin exchange operators. By making use of the identities

$$P^{\mathrm{space}}(\mathbf{K}_1 - \mathbf{K}_2) = -(\mathbf{k}_1 - \mathbf{k}_2)/2, \tag{A4}$$

$$P^{\sigma}\boldsymbol{\sigma}_1\cdot\boldsymbol{\sigma}_2 = (3 - \boldsymbol{\sigma}_1\cdot\boldsymbol{\sigma}_2)/2, \tag{A5}$$

$$P^{\tau}(\tau_{1,z} - \tau_{2,z}) = i\,(\boldsymbol{\tau}_1\times\boldsymbol{\tau}_2)_z, \tag{A6}$$

$$\begin{aligned}&P^{\sigma}\,P^{\mathrm{space}}[\boldsymbol{\sigma}_1\cdot(\mathbf{K}_1 - \mathbf{K}_2)\,\boldsymbol{\sigma}_2 + \boldsymbol{\sigma}_2\cdot(\mathbf{K}_1 - \mathbf{K}_2)\,\boldsymbol{\sigma}_1]\\ &= -\tfrac{1}{2}[(\mathbf{k}_1 - \mathbf{k}_2)(1 - \boldsymbol{\sigma}_1\cdot\boldsymbol{\sigma}_2) + \boldsymbol{\sigma}_1\cdot(\mathbf{k}_1 - \mathbf{k}_2)\,\boldsymbol{\sigma}_2\\ &\quad + \boldsymbol{\sigma}_2\cdot(\mathbf{k}_1 - \mathbf{k}_2)\,\boldsymbol{\sigma}_1],\end{aligned} \tag{A7}$$

Eq. (2.20) in the text follows.

An alternative way to proceed is to express the original set of LECs $C'_1, \ldots, C'_{14}$ entering Eq. (3.11) of Ref. [5] in terms of the twelve independent LECs $C_1, \ldots, C_7, C^*_1, \ldots, C^*_5$ (in the notation of Ref. [5]), and then to set the $C^*_i = 0$, that is, to ignore the currents induced by these terms, since they are suppressed by $1/m_N^2$. Substituting

$$\begin{aligned}&C'_1 = \tfrac{1}{2}C_1, \quad C'_2 = C_1 - \tfrac{1}{4}C_2, \quad C'_3 = -\tfrac{1}{8}C_2,\\ &C'_4 + C'_6 = -\tfrac{1}{4}C_5, \quad C'_5 + C'_6 = 0,\\ &C'_7 + \tfrac{1}{2}C'_{11} = \tfrac{1}{2}C_6 + \tfrac{1}{16}C_7, \quad C'_8 - \tfrac{1}{2}C'_{11} = \tfrac{1}{16}C_7,\\ &C'_9 = \tfrac{1}{2}C_3 + \tfrac{1}{8}C_4, \quad C'_{10} + C'_{11} = C_6, \quad C'_{12} = C_3,\\ &C'_{13} = \tfrac{1}{8}C_7, \quad C'_{14} = \tfrac{1}{8}C_4\end{aligned} \tag{A8}$$

into Eq. (3.11) of Ref. [5], we find

$$\begin{aligned}&\text{Eq. (3.11) of Ref.[1]}\\ &\quad = \text{Eq. (A2)} - i\,e\,C'_4\,(e_1 + e_2)(\boldsymbol{\sigma}_1 + \boldsymbol{\sigma}_2)\times\mathbf{q},\end{aligned} \tag{A9}$$

and the difference can be absorbed into a redefinition of C'_{15}, since $(\tau^z_1 + \tau^z_2)(\boldsymbol{\sigma}_1 + \boldsymbol{\sigma}_2)\times\mathbf{q} = 0$ after antisymmetrization. Notice also that, in view of the identity $O_4 + O_5 = O_6 + O_{15}$ (which was derived in Ref. [69], and, apart from O_{15}, of no relevance there), among the operators of the subleading contact Lagrangian, the operator O_6 is redundant, and indeed the dependence on the associated LEC C'_6 cancels in the observables.

APPENDIX B: ONE-LOOP SHORT-RANGE CURRENT AND CHARGE OPERATORS

In this Appendix, we discuss the contributions associated with panels (h)–(k) in Fig. 2 for the current operator and (g)–(j) in Fig. 3 for the charge operator. We begin with the current operator. The contributions of diagrams (h) and (j) in Fig. 2 vanish, while the contribution of diagrams of type (i) was obtained as (with conventions for $\mathbf{q}$ integrations and $\overline{\delta}$ functions being the same as in Ref. [5])

$$\begin{aligned}\mathbf{j}^{(1)}_{\mathrm{i}} = &\,2\,i\,\frac{e\,g_A^2\,C_T}{F_\pi^2}\,(\boldsymbol{\tau}_1\times\boldsymbol{\tau}_2)_z\int_{\mathbf{q}_1,\mathbf{q}_2}\overline{\delta}(\mathbf{q}_1 + \mathbf{q}_2 - \mathbf{q})\\ &\times\overline{D}(\omega_1,\omega_2)\,(\mathbf{q}_1 - \mathbf{q}_2)\,\boldsymbol{\sigma}_1\cdot\mathbf{q}_2\,\boldsymbol{\sigma}_2\cdot\mathbf{q}_1,\end{aligned} \tag{B1}$$

where

$$\overline{D}(\omega_1,\omega_2) = \frac{\omega_1^2 + \omega_1\omega_2 + \omega_2^2}{\omega_1^3\omega_2^3(\omega_1 + \omega_2)}. \tag{B2}$$

Before analyzing diagram (k), we need to consider the leading and next-to-leading contributions to the single-nucleon diagrams shown in Fig. 12. For simplicity, we define the vertices

$$V_1 = i\,\frac{g_A}{F_\pi}\,\boldsymbol{\sigma}\cdot\mathbf{q}_1\,\tau_a, \quad V_2 = i\,\frac{g_A}{F_\pi}\,\boldsymbol{\sigma}\cdot\mathbf{q}_2\,\tau_b, \tag{B3}$$

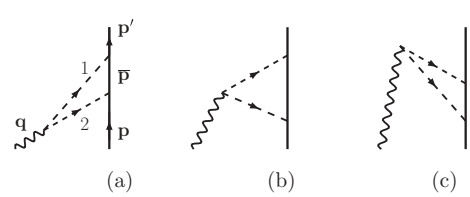

FIG. 12. Time-ordered diagrams illustrating one of the classes of loop corrections to the single-nucleon current. Nucleons, pions, and photons are denoted by solid, dashed, and wavy lines, respectively.

$$V_\gamma = -i\, e\, \epsilon_{abz}\, (\mathbf{q}_1 - \mathbf{q}_2). \tag{B4}$$

Then the current reads

$$\mathbf{j}_{\gamma\pi\pi} = \frac{V_1 V_2 V_\gamma}{4\,\omega_1\omega_2}\Bigg[\frac{1}{E_i-\omega_1-\overline{E}}\,\frac{1}{E_i-\omega_1-\omega_2-E} + \frac{1}{E_i-\omega_1-\overline{E}}\,\frac{1}{E_i-\omega_\gamma-\omega_2-\overline{E}} + \frac{1}{E_i-\omega_\gamma-\omega_1-\omega_2-E'}\,\frac{1}{E_i-\omega_\gamma-\omega_2-\overline{E}}\Bigg], \tag{B5}$$

where $E_i = E + \omega_\gamma$ and $\overline{E}$ is the energy of the intermediate nucleon of momentum $\overline{\mathbf{p}}$. After expanding the energy denominators as in Eq. (2.18) to include linear terms in the nucleon kinetic energies, we find, up to next-to-leading order included,

$$\mathbf{j}_{\gamma\pi\pi} = \frac{V_1 V_2 V_\gamma}{4}\Bigg[\frac{2}{\omega_1^2\omega_2^2} + D'(\omega_1,\omega_2)\,(E'-\overline{E}) + D(\omega_1,\omega_2)(E-\overline{E}) + D_\gamma(\omega_1,\omega_2)\,\omega_\gamma\Bigg], \tag{B6}$$

where

$$D(\omega_1,\omega_2) = \frac{2\,\omega_1+\omega_2}{\omega_1^2\omega_2^3(\omega_1+\omega_2)}, \tag{B7}$$

$$D'(\omega_1,\omega_2) = \frac{\omega_1+2\,\omega_2}{\omega_1^3\omega_2^2(\omega_1+\omega_2)}, \tag{B8}$$

$$D_\gamma(\omega_1,\omega_2) = -\frac{\omega_1-\omega_2}{\omega_1^2\omega_2^2\,(\omega_1+\omega_2)^2}, \tag{B9}$$

and

$$D \rightleftharpoons D' \quad \text{with} \quad \mathbf{q}_1 \rightleftharpoons \mathbf{q}_2, \quad D + D' = 2\,\overline{D}. \tag{B10}$$

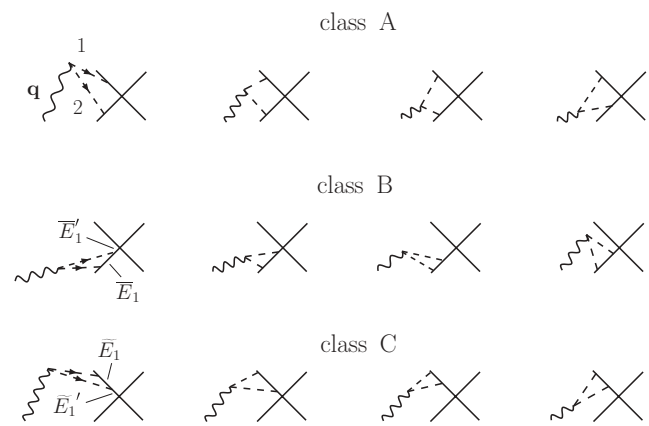

FIG. 13. Set of time-ordered diagrams for the contribution illustrated by the single diagram (k) in Fig. 2. The notation is the same as in Fig. 12.

We now proceed to analyze the contributions of diagrams of type (k) in Fig. 2. To this end, we show in Fig. 13 the complete set of time-ordered diagrams of the same topology as (k), which we have separated for convenience into the three classes A, B, and C. Class A consists only of irreducible diagrams, which at order $n = 1$ or eQ, i.e., in the static limit, lead to

$$\begin{aligned}\text{class A} &= -\tfrac{1}{2}\, V_\gamma V_1 V_{\rm CT} V_2 \overline{D}(\omega_1,\omega_2)\\ &= -\tfrac{1}{4} V_\gamma V_1 V_{\rm CT} V_2 [D(\omega_1,\omega_2) + D'(\omega_1,\omega_2)],\end{aligned} \tag{B11}$$

where the vertices V_1, V_2, and V_γ are defined as above (with the spin and isospin matrices now referring to nucleon 1), and

$$V_{\rm CT} = C_S + C_T\, \boldsymbol{\sigma}_1\cdot\boldsymbol{\sigma}_2. \tag{B12}$$

On the other hand, to order eQ included, class B gives

$$\text{class B} = \frac{V_\gamma V_{\rm CT} V_1 V_2}{4\,\omega_1\omega_2}\,\frac{1}{E_i-\overline{E}_1'-E_2}\Bigg[\frac{1}{\omega_1(\omega_1+\omega_2)}\Bigg(1+\frac{E_1+\omega_\gamma-\overline{E}_1}{\omega_1}+\frac{\omega_\gamma}{\omega_1+\omega_2}\Bigg)+\frac{1}{\omega_1\omega_2}\Bigg(1+\frac{E_1+\omega_\gamma-\overline{E}_1}{\omega_1} + \frac{E_1-\overline{E}_1}{\omega_2}\Bigg)+\frac{1}{\omega_2(\omega_1+\omega_2)}\Bigg(1+\frac{E_i-\overline{E}_1'-E_2}{\omega_1+\omega_2}-\frac{\omega_\gamma}{\omega_1+\omega_2}+\frac{E_1-\overline{E}_1}{\omega_2}\Bigg)\Bigg] - \frac{V_\gamma V_{\rm CT} V_1 V_2}{4\,\omega_1\omega_2}\,\frac{1}{\omega_2(\omega_1+\omega_2)^2}, \tag{B13}$$

where we have used energy conservation between the initial and final states, $E_1 + E_2 + \omega_\gamma = E_1' + E_2'$. We now note that the irreducible contribution from the last diagram (in class B) is canceled by the second term in the next to last line of the above equation, so that we are left with

$$\begin{aligned}\text{class B} &= \frac{V_\gamma V_{\rm CT} V_1 V_2}{4}\,\frac{1}{E_i-\overline{E}_1'-E_2}\Bigg[\frac{2}{\omega_1^2\omega_2^2} + \omega_\gamma\, D_\gamma(\omega_1,\omega_2) + (E_1-\overline{E}_1)\, D(\omega_1,\omega_2) + (E_1+\omega_\gamma-\overline{E}_1)\, D'(\omega_1,\omega_2)\Bigg]\\ &= V_{\rm CT}\,\frac{1}{E_i-\overline{E}_1'-E_2}\,\mathbf{j}_{\gamma\pi\pi} + \frac{V_\gamma V_{\rm CT} V_1 V_2}{4}\, D'(\omega_1,\omega_2),\end{aligned} \tag{B14}$$

since $E_1 + \omega_\gamma - \overline{E}_1 = (E_i - \overline{E}_1' - E_2) + (\overline{E}_1' - \overline{E}_1)$ and V_γ commutes with each of the remaining vertices. The first term represents an iteration, while the recoil-corrected class B contribution is simply given by $V_\gamma V_{\rm CT} V_1 V_2\, D'(\omega_1, \omega_2)/4$. A similar analysis for class C leads to the recoil-corrected class C contribution given by $V_\gamma V_1 V_2 V_{\rm CT}\, D(\omega_1, \omega_2)/4$. Therefore combining the contributions from classes A, B, and C, we find

$$\mathbf{j}_{\rm k}^{(1)} = \tfrac{1}{4} V_\gamma V_1\, [V_2, V_{\rm CT}]\, D(\omega_1, \omega_2) + \tfrac{1}{4}[V_{\rm CT}, V_1]\, V_2\, V_\gamma\, D'(\omega_1, \omega_2), \tag{B15}$$

or explicitly

$$\mathbf{j}_{\rm k}^{(1)} = 2\, i\, \frac{e\, g_A^2\, C_T}{F_\pi^2}\, \tau_{1z} \int_{\mathbf{q}_1, \mathbf{q}_2} \overline{\delta}(\mathbf{q}_1 + \mathbf{q}_2 - \mathbf{q})\, \overline{D}(\omega_1, \omega_2) \times (\mathbf{q}_1 - \mathbf{q}_2)\, \boldsymbol{\sigma}_2 \cdot \mathbf{q}_2 \times \mathbf{q}_1 + 1 \rightleftharpoons 2. \tag{B16}$$

The currents $\mathbf{j}_{\rm i}^{(1)}$ and $\mathbf{j}_{\rm k}^{(1)}$ obtained here are in agreement with those in Eq. (5.2) of Ref. [8], except for an overall factor of 2. Ultimately, this difference has no impact, since

$$\mathbf{j}_{\rm i}^{(1)} + \mathbf{j}_{\rm k}^{1)} \propto (\boldsymbol{\tau}_1 \times \boldsymbol{\tau}_2)_z\, (\boldsymbol{\sigma}_1 \times \boldsymbol{\sigma}_2) \times \mathbf{q} + \left(2\, \tau_{1z}\, \boldsymbol{\sigma}_2 + 2\, \tau_{2z}\, \boldsymbol{\sigma}_1\right) \times \mathbf{q} = 0, \tag{B17}$$

which vanishes due to antisymmetry of the two-nucleon states.

In Ref. [5] we had not considered the next-to-leading order contributions to the single-nucleon $\gamma\pi\pi$ vertex when deriving the one-loop correction to the OPE current shown in Fig. 14 (see Appendix E of Ref. [5]). As a consequence we had failed to isolate the correct noniterative piece, which had led, in particular, to a non-Hermitian operator. We find that this term is now given by

$$\mathbf{j}_{\rm OPE,loop}^{(1)} = i e \frac{g_A^4}{F_\pi^4} (\boldsymbol{\tau}_1 \times \boldsymbol{\tau}_2)_z \frac{\boldsymbol{\sigma}_2 \cdot \mathbf{k}_2}{\omega_{k_2}^2} \int_{\mathbf{p}} \mathbf{p} \left[2 \frac{\omega_+^2 + \omega_-^2 + \omega_+ \omega_-}{\omega_+^3 \omega_-^3 (\omega_+ + \omega_-)} \times (\boldsymbol{\sigma}_1 \cdot \mathbf{q}\, \mathbf{k}_2 \cdot \mathbf{p} - \boldsymbol{\sigma}_1 \cdot \mathbf{p}\, \mathbf{k}_2 \cdot \mathbf{q}) - \frac{\omega_+ - \omega_-}{\omega_+^3 \omega_-^3}\, \boldsymbol{\sigma}_1 \cdot \mathbf{k}_2\, (q^2 - p^2) \right] + 1 \rightleftharpoons 2, \tag{B18}$$

where $\omega_\pm = \sqrt{(\mathbf{q} \pm \mathbf{p})^2 + 4\, m_\pi^2}$.

Next, we turn our attention to the charge operator. In Ref. [6] we showed that the contributions of diagrams (g) and (h) in Fig. 3 vanish. However, in light of the previous considerations, those due to diagrams (i) and (j) given there need to be revised. Indeed, an analysis similar to that carried out above leads to the single-nucleon charge operator (see Fig. 12), up to next-to-leading order included,

$$\rho_{\gamma\pi\pi} = \frac{V_1 V_2 \widetilde{V}_\gamma}{4} \left[\frac{4}{\omega_1\, \omega_2\, (\omega_1 + \omega_2)} + \widetilde{D}'(\omega_1, \omega_2)\, (E' - \overline{E}) + \widetilde{D}(\omega_1, \omega_2)(E - \overline{E}) + \widetilde{D}_\gamma(\omega_1, \omega_2)\, \omega_\gamma \right] \tag{B19}$$

and to a contribution for diagram (j) (see Fig. 13) which reads

$$\rho_{\rm j}^{(1)} = -2\, \frac{e\, g_A^2\, C_T}{F_\pi^2}\, \tau_{1z} \int_{\mathbf{q}_1, \mathbf{q}_2} \overline{\delta}(\mathbf{q}_1 + \mathbf{q}_2 - \mathbf{q})\, \widetilde{D}(\omega_1, \omega_2) \times \boldsymbol{\sigma}_1 \cdot [\mathbf{q}_1 \times (\boldsymbol{\sigma}_2 \times \mathbf{q}_2)] + 1 \rightleftharpoons 2. \tag{B20}$$

We have defined $\widetilde{V}_\gamma = -i\, e\, \epsilon_{abz}$, and

$$\widetilde{D}(\omega_1, \omega_2) = \frac{3\, \omega_1 + \omega_2}{\omega_1^2\, \omega_2^2\, (\omega_1 + \omega_2)}, \tag{B21}$$

$$\widetilde{D}'(\omega_1, \omega_2) = \frac{\omega_1 + 3\, \omega_2}{\omega_1^2\, \omega_2^2\, (\omega_1 + \omega_2)}, \tag{B22}$$

$$\widetilde{D}_\gamma(\omega_1, \omega_2) = \frac{\omega_1 - \omega_2}{\omega_1^2\, \omega_2^2\, (\omega_1 + \omega_2)^2}, \tag{B23}$$

with

$$\widetilde{D} \rightleftharpoons \widetilde{D}' \quad \text{with} \quad \mathbf{q}_1 \rightleftharpoons \mathbf{q}_2, \quad \widetilde{D} + \widetilde{D}' = \frac{4}{\omega_1^2\, \omega_2^2}. \tag{B24}$$

We now revise the derivation of the charge operator of type (i) illustrated in Fig. 3. The associated time-ordered diagrams are represented in Fig. 15, and they have been separated into three classes. In Ref. [6], the expression reported in Eq. (53) has been obtained by accounting for the recoil-corrected class A diagrams only, i.e.,

$$\begin{aligned} \text{class A} &= \frac{1}{2\, \omega_1^4} [V_1 V_{\rm CT} V_1' V_\gamma' + V_\gamma' V_1 V_{\rm CT} V_1' - V_1 V_{\rm CT} V_\gamma' V_1' - V_1 V_\gamma' V_{\rm CT} V_1'] \\ &= e\, \frac{2\, g_A^2}{3\, F_\pi^2}\, \tau_{1,z}\, (3\, C_S - C_T\, \boldsymbol{\sigma}_1 \cdot \boldsymbol{\sigma}_2) \int_{\mathbf{q}_1} \frac{q_1^2}{\omega_1^4}, \end{aligned} \tag{B25}$$

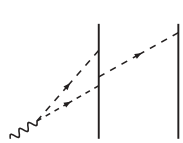

FIG. 14. One-loop correction to the OPE current (with only one among the possible time orderings being shown). The notation is the same as in Fig. 12.

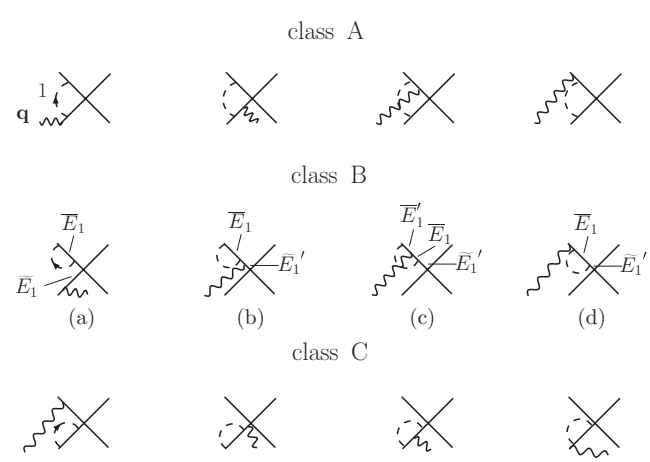

FIG. 15. Set of time-ordered diagrams for the contribution illustrated by the single diagram (i) in Fig. 3. The notation is the same as in Fig. 12.

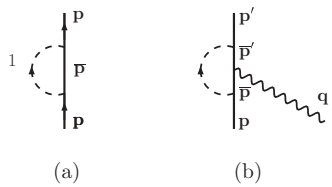

FIG. 16. Diagrams for the single-nucleon contributions. The notation is the same as in Fig. 12.

where V_1 and $V_{\rm CT}$ are given in Eqs. (B3) and (B12), respectively, and V_1' and V_γ' are defined as

$$V_1' = -V_1, \quad V_\gamma' = \frac{e}{2}(1+\tau_{1,z}). \tag{B26}$$

Classes B and C involve only reducible diagrams. First, we analyze the single-nucleon contributions entering the reducible diagrams, represented in Fig. 16. We account for leading, next-to-leading, and next-to-next-to-leading order corrections in the expansion of the energy denominators. The contributions M_N and ρ_γ, associated with panels (a) and (b), respectively, read

$$M_N = -\frac{V_1\,V_1'}{2\,\omega_1^2}\left[1+\frac{E-\overline{E}}{\omega_1}+\frac{(E-\overline{E})^2}{\omega_1^2}\right], \tag{B27}$$

$$\rho_\gamma = \frac{V_1\,V_\gamma'\,V_1'}{2\,\omega_1^3}\left(1+\frac{E'-\overline{E}'}{\omega_1}+\frac{E-\overline{E}}{\omega_1}\right), \tag{B28}$$

where the energies are as indicated in Fig. 16, and energy conservation ($E+\omega_\gamma = E'$) has been used. In terms of these, the contributions of diagram (a) and (b) in class B are given by

$$B_{\rm a} = M_N\,\frac{1}{E_i-E_1'-E_2'}\,V_{\rm CT}\,\frac{1}{E_i-\widetilde{E}_1-E_2}\,V_\gamma', \tag{B29}$$

$$B_{\rm b} = M_N\,\frac{1}{E_i-E_1'-E_2'}\,V_\gamma'\,\frac{1}{E_i-\widetilde{E}_1'-E_2'-\omega_\gamma}\,V_{\rm CT}, \tag{B30}$$

where we have identified and isolated the nucleon self-energy terms (to be reabsorbed by mass counterterms). Evaluation of panel (c) leads to

$$\begin{aligned} B_{\rm c} &= \frac{V_1\,V_\gamma'\,V_1'}{2\,\omega_1^3}\left[1+\frac{E_1'-\overline{E}_1'}{\omega_1}+\frac{\widetilde{E}_1'-\overline{E}_1}{\omega_1}\right] \\ &\quad\times\frac{1}{E_i-\widetilde{E}_1'-E_2'-\omega_\gamma}\,V_{\rm CT}+\frac{V_1\,V_\gamma'\,V_1'V_{\rm CT}}{2\,\omega_1^4} \\ &= \rho_\gamma\,\frac{1}{E_i-\widetilde{E}_1'-E_2'-\omega_\gamma}\,V_{\rm CT}+\frac{V_1\,V_\gamma'\,V_1'V_{\rm CT}}{2\,\omega_1^4}, \end{aligned} \tag{B31}$$

where the first term represents an iteration with ρ_γ and the contact interaction, and the second term is the recoil correction contributing to the two-nucleon charge operator. Finally, the contribution of panel (d), in which, in contrast to panels (a) and (b), the self-energy insertion is between the photon absorption and contact interaction, is expressed as

$$\begin{aligned} B_{\rm d} &= -V_\gamma'\,\frac{1}{E_i-\widetilde{E}_1'-E_2'-\omega_\gamma}\,\frac{V_1\,V_1'}{2\,\omega_1^2}\left[1+\frac{\widetilde{E}_1'-\overline{E}_1}{\omega_1}+\frac{(\widetilde{E}_1'-\overline{E}_1)^2}{\omega_1^2}\right]\frac{1}{E_i-\widetilde{E}_1'-E_2'-\omega_\gamma}\,V_{\rm CT} \\ &\quad-\frac{V_\gamma'V_1\,V_1'}{2\,\omega_1^3}\left(1+2\,\frac{\widetilde{E}_1'-\overline{E}_1}{\omega_1}\right)\frac{1}{E_i-\widetilde{E}_1'-E_2'-\omega_\gamma}V_{\rm CT}-\frac{V_\gamma'V_1\,V_1'V_{\rm CT}}{2\,\omega_1^4} \\ &= V_\gamma'\,\frac{1}{E_i-\widetilde{E}_1'-E_2'-\omega_\gamma}\,M_N\,\frac{1}{E_i-\widetilde{E}_1'-E_2'-\omega_\gamma}\,V_{\rm CT}+\widetilde{\rho}_\gamma\,\frac{1}{E_i-\widetilde{E}_1'-E_2'-\omega_\gamma}\,V_{\rm CT}-\frac{V_\gamma'V_1\,V_1'V_{\rm CT}}{2\,\omega_1^4}, \end{aligned} \tag{B32}$$

where the last term is a two-nucleon term, and we interpret $\widetilde{\rho}_\gamma$ as a further correction to the single-nucleon γN vertex. However, the analysis and proper interpretation of these types of corrections are beyond the scope of the present work.

After a similar analysis of the class C diagrams is carried out, we find that the complete B + C contribution reads

$$\begin{aligned} \text{classes B}+\text{C} &= \frac{1}{2\,\omega_1^4}[V_1V_\gamma'\,V_1'V_{\rm CT}-V_\gamma'V_1\,V_1'V_{\rm CT}+V_{\rm CT}V_1V_\gamma'\,V_1'-V_{\rm CT}V_1V_1'V_\gamma'] \\ &= -e\,\frac{2\,g_A^2}{F_\pi^2}\,\tau_{1,z}\,(C_S+C_T\,\boldsymbol{\sigma}_1\cdot\boldsymbol{\sigma}_2)\int_{\mathbf{q}_1}\frac{q_1^2}{\omega_1^4}, \end{aligned} \tag{B33}$$

which combined with Eq. (B25) leads to the type (i) charge operator in Fig. 3,

$$\rho_{\rm i}^{(1)} = -e\,\frac{8\,g_A^2\,C_T}{3\,F_\pi^2}\,\tau_{1,z}\,\boldsymbol{\sigma}_1\cdot\boldsymbol{\sigma}_2\int_{\mathbf{q}_1}\frac{q_1^2}{\omega_1^4}+1\rightleftharpoons 2. \tag{B34}$$

APPENDIX C: LOOP INTEGRATIONS

In this Appendix, we outline the derivation of the two-body charge operators at one loop listed in Sec. II B. For the sake of illustration, we consider the contribution of panel (f) in Fig. 3, given by (in the notation of

Ref. [6])

$$\rho_{\rm f}^{(1)} = -e\,\frac{2\,g_A^4}{F_\pi^4}\int_{\mathbf{q}_1,\mathbf{q}_2,\mathbf{q}_3}\bar{\delta}(\mathbf{q}_2+\mathbf{q}_3-\mathbf{k}_2)\bar{\delta}(\mathbf{q}_1-\mathbf{q}_2-\mathbf{k}_1)\bar{\delta}(\mathbf{q}_1+\mathbf{q}_3-\mathbf{q})\,\frac{1}{\omega_1^2\,\omega_2^2\,\omega_3^2}\,[2\,\tau_{1,z}\,(\mathbf{q}_2\cdot\mathbf{q}_1\;\mathbf{q}_2\cdot\mathbf{q}_3 - \boldsymbol{\sigma}_1\cdot\mathbf{q}_2\times\mathbf{q}_1\;\boldsymbol{\sigma}_2\cdot\mathbf{q}_3\times\mathbf{q}_2) - (\boldsymbol{\tau}_1\times\boldsymbol{\tau}_2)_z\;\mathbf{q}_1\cdot\mathbf{q}_2\,\boldsymbol{\sigma}_2\cdot\mathbf{q}_3\times\mathbf{q}_2] + 1 \rightleftharpoons 2, \tag{C1}$$

which can conveniently be written as

$$\rho_{\rm f}^{(1)} = -e\,\frac{2\,g_A^4}{F_\pi^4}\int_{\mathbf{p}}\frac{N(\mathbf{q},\mathbf{k},\mathbf{p})}{\omega^2_{\mathbf{q}/2+\mathbf{p}}\,\omega^2_{\mathbf{q}/2-\mathbf{p}}\,\omega^2_{\mathbf{p}-\mathbf{k}}} + 1 \rightleftharpoons 2, \tag{C2}$$

with

$$N(\mathbf{q},\mathbf{k},\mathbf{p}) = 2\,\tau_{1,z}[(\mathbf{p}-\mathbf{k})\cdot(\mathbf{q}/2+\mathbf{p})(\mathbf{p}-\mathbf{k})\cdot(\mathbf{q}/2-\mathbf{p}) - \boldsymbol{\sigma}_1\cdot(\mathbf{p}-\mathbf{k})\times(\mathbf{q}/2+\mathbf{p})\;\boldsymbol{\sigma}_2\cdot(\mathbf{q}/2-\mathbf{p})\times(\mathbf{p}-\mathbf{k})] - (\boldsymbol{\tau}_1\times\boldsymbol{\tau}_2)_z\;(\mathbf{q}/2+\mathbf{p})\cdot(\mathbf{p}-\mathbf{k})\,\boldsymbol{\sigma}_2\cdot(\mathbf{q}/2-\mathbf{p})\times(\mathbf{p}-\mathbf{k}) \tag{C3}$$

and the momentum $\mathbf{k}$ defined as in Eq. (2.2). We now use standard techniques [70] to express the product of energy denominators in the following way:

$$\frac{1}{\omega^2_{\mathbf{q}/2+\mathbf{p}}\,\omega^2_{\mathbf{q}/2-\mathbf{p}}\,\omega^2_{\mathbf{p}-\mathbf{k}}} = 2\int_0^1 dz_1\int_0^{1-z_1} dz_2\big\{\big[(\mathbf{q}/2+\mathbf{p})^2+m_\pi^2\big]z_1 + \big[(\mathbf{q}/2-\mathbf{p})^2+m_\pi^2\big]z_2 + \big[(\mathbf{p}-\mathbf{k})^2+m_\pi^2\big]\,(1-z_1-z_2)\big\}^{-3}, \tag{C4}$$

which, in terms of

$$\mathbf{p}' = \mathbf{p} + (z_1-z_2)\,\mathbf{q}/2 - (1-z_1-z_2)\,\mathbf{k}, \tag{C5}$$

simply reads

$$\frac{1}{\omega^2_{\mathbf{q}/2+\mathbf{p}}\,\omega^2_{\mathbf{q}/2-\mathbf{p}}\,\omega^2_{\mathbf{p}-\mathbf{k}}} = 2\int_0^1 dz_1\int_0^{1-z_1} dz_2\,[p'^2+\lambda^2(z_1,z_2)]^{-3}, \tag{C6}$$

where

$$\lambda^2(z_1,z_2) = (z_1+z_2)\mathbf{q}^2/4 - [(z_1-z_2)\mathbf{q}/2 - (1-z_1-z_2)\,\mathbf{k}]^2 + (1-z_1-z_2)\,\mathbf{k}^2 + m_\pi^2. \tag{C7}$$

After these manipulations, the charge operator can finally be written as

$$\rho_{\rm f}^{(1)} = -e\,\frac{4\,g_A^4}{F_\pi^4}\int_0^1 dx\,x\int_{-1/2}^{1/2} dy\int_{\mathbf{p}'} N'(\mathbf{q},\mathbf{k},\mathbf{p}')[p'^2+\lambda^2(x,y)]^{-3} + 1 \rightleftharpoons 2, \tag{C8}$$

where the function N' is obtained from N by expressing $\mathbf{p}$ in terms of $\mathbf{p}'$ via Eq. (C5). We have also changed variables in the parametric integrals by introducing [70]

$$x = z_1+z_2, \quad x\,y = (z_1-z_2)/2, \tag{C9}$$

such that

$$\int_0^1 dz_1\int_0^{1-z_1} dz_2 \longrightarrow \int_0^1 dx\,x\int_{-1/2}^{1/2} dy. \tag{C10}$$

The function N' is a polynomial in $\mathbf{p}'$, and the $\mathbf{p}'$ integrations are carried out in dimensional regularization (see Appendix A of Ref. [5]). They are finite and lead to the charge operator given in Eq. (2.38).

[1] S. Weinberg, Phys. Lett. B **251**, 288 (1990); Nucl. Phys. B **363**, 3 (1991); Phys. Lett. B **295**, 114 (1992).
[2] P. F. Bedaque and U. van Kolck, Ann. Rev. Nucl. Part. Sci. **52**, 339 (2002).
[3] E. Epelbaum, H. W. Hammer, and U.-G. Meissner, Rev. Mod. Phys. **81**, 1773 (2009).
[4] T.-S. Park, D.-P. Min, and M. Rho, Nucl. Phys. A **596**, 515 (1996).
[5] S. Pastore, L. Girlanda, R. Schiavilla, M. Viviani, and R. B. Wiringa, Phys. Rev. C **80**, 034004 (2009).
[6] S. Pastore, L. Girlanda, R. Schiavilla, and M. Viviani, Phys. Rev. C **84**, 024001 (2011).
[7] S. Kölling, E. Epelbaum, H. Krebs, and U.-G. Meissner, Phys. Rev. C **80**, 045502 (2009).
[8] S. Kölling, E. Epelbaum, H. Krebs, and U.-G. Meissner, Phys. Rev. C **84**, 054008 (2011).
[9] M. Walzl and U.-G. Meissner, Phys. Lett. B **513**, 37 (2001).
[10] D. R. Phillips, Phys. Lett. B **567**, 12 (2003).
[11] D. R. Phillips, J. Phys. G **34**, 365 (2007).

[12] S. Kölling, E. Epelbaum, and D. R. Phillips, Phys. Rev. C **86**, 047001 (2012).
[13] C. E. Hyde-Wright and K. de Jager, Annu. Rev. Nucl. Part. Sci. **54**, 217 (2004).
[14] G. Höhler *et al.*, Nucl. Phys. B **114**, 505 (1976).
[15] B. Kubis and U.-G. Meissner, Nucl. Phys. A **679**, 698 (2001).
[16] J. Carlson and R. Schiavilla, Rev. Mod. Phys. **70**, 743 (1998).
[17] D. O. Riska, Phys. Rep. **181**, 207 (1989).
[18] J. L. Friar, Ann. Phys. (NY) **104**, 380 (1977); Phys. Rev. C **22**, 796 (1980).
[19] R. B. Wiringa, V. G. J. Stoks, and R. Schiavilla, Phys. Rev. C **51**, 38 (1995).
[20] D. R. Entem and R. Machleidt, Phys. Rev. C **68**, 041001 (2003); R. Machleidt and D. R. Entem, Phys. Rep. **503**, 1 (2011).
[21] C. E. Carlson, Phys. Rev. D **34**, 2704 (1986).
[22] L. Girlanda, A. Kievsky, L. E. Marcucci, S. Pastore, R. Schiavilla, and M. Viviani, Phys. Rev. Lett. **105**, 232502 (2010).
[23] R. Schiavilla and V. R. Pandharipande, Phys. Rev. C **65**, 064009 (2002).
[24] R. Schiavilla, V. R. Pandharipande, and D. O. Riska, Phys. Rev. C **40**, 2294 (1989).
[25] A. Kievsky, L. E. Marcucci, S. Rosati, and M. Viviani, Few-Body Syst. **22**, 1 (1997).
[26] M. Viviani, L. E. Marcucci, S. Rosati, A. Kievsky, and L. Girlanda, Few-Body Syst. **39**, 159 (2006).
[27] A. Kievsky, S. Rosati, M. Viviani, L. E. Marcucci, and L. Girlanda, J. Phys. G **35**, 063101 (2008).
[28] L. E. Marcucci, A. Kievsky, L. Girlanda, S. Rosati, and M. Viviani, Phys. Rev. C **80**, 034003 (2009).
[29] J. J. de Swart, M. C. M. Rentmeester, and R. G. E. Timmermans, PiN Newslett. **13**, 96 (1997).
[30] B. S. Pudliner, V. R. Pandharipande, J. Carlson, and R. B. Wiringa, Phys. Rev. Lett. **74**, 4396 (1995).
[31] P. Navratil, Few-Body Syst. **41**, 117 (2007).
[32] L. E. Marcucci, A. Kievsky, S. Rosati, R. Schiavilla, and M. Viviani, Phys. Rev. Lett. **108**, 052502 (2012).
[33] T.-S. Park *et al.*, Phys. Lett. B **472**, 232 (2000); Y.-H. Song *et al.*, *ibid.* **656**, 174 (2007); Y.-H. Song, R. Lazauskas, and T.-S. Park, Phys. Rev. C **79**, 064002 (2009); R. Lazauskas, Y.-H. Song, and T.-S. Park, *ibid.* **83**, 034006 (2011).
[34] P. J. Mohr and B. N. Taylor, Rev. Mod. Phys. **77**, 1 (2005).
[35] D. M. Bishop and L. M. Cheung, Phys. Rev. A **20**, 381 (1979).
[36] C. D. Buchanan and M. R. Yearian, Phys. Rev. Lett. **15**, 303 (1965).
[37] D. Benaksas, D. Drickey, and D. Frèrejacque, Phys. Rev. **148**, 1327 (1966).
[38] J. E. Elias *et al.*, Phys. Rev. **177**, 2075 (1969).
[39] S. Galster *et al.*, Nucl. Phys. B **32**, 221 (1971).
[40] R. W. Berard *et al.*, Phys. Lett. B **47**, 355 (1973).
[41] R. G. Arnold *et al.*, Phys. Rev. Lett. **35**, 776 (1975).
[42] G. G. Simon, C. Schmitt, and V. H. Walther, Nucl. Phys. A **364**, 285 (1981).
[43] R. Cramer *et al.*, Z. Phys. C **29**, 513 (1985).
[44] S. Platchkov *et al.*, Nucl. Phys. A **510**, 740 (1990).
[45] D. Abbott *et al.*, Phys. Rev. Lett. **82**, 1379 (1999).
[46] L. C. Alexa *et al.*, Phys. Rev. Lett. **82**, 1374 (1999).
[47] M. E. Schulze *et al.*, Phys. Rev. Lett. **52**, 597 (1984).
[48] I. The *et al.*, Phys. Rev. Lett. **67**, 173 (1991).
[49] C. Zhang *et al.*, Phys. Rev. Lett. **107**, 252501 (2011).
[50] V. F. Dmitriev *et al.*, Phys. Lett. B **157**, 143 (1985).
[51] B. B. Wojtsekhowski *et al.*, Pis'ma Zh. Eksp. Teor. Fiz. **43**, 567 (1986) [JETP Lett. **43**, 733 (1986)].
[52] R. Gilman *et al.*, Phys. Rev. Lett. **65**, 1733 (1990).
[53] D. M. Nikolenko *et al.*, Phys. Rev. Lett. **90**, 072501 (2003).
[54] B. Boden *et al.*, Z. Phys. C **49**, 175 (1991).
[55] M. Ferro-Luzzi *et al.*, Phys. Rev. Lett. **77**, 2630 (1996).
[56] M. Bouwhuis *et al.*, Phys. Rev. Lett. **82**, 3755 (1999).
[57] D. Abbott *et al.*, Phys. Rev. Lett. **84**, 5053 (2000).
[58] S. Auffret *et al.*, Phys. Rev. Lett. **54**, 649 (1985).
[59] P. E. Bosted *et al.*, Phys. Rev. C **42**, 38 (1990).
[60] I. Sick, Prog. Part. Nucl. Phys. **47**, 245 (2001).
[61] A. Amroun *et al.*, Nucl. Phys. A **579**, 596 (1994).
[62] E. Epelbaum, W. Glöckle, and U.-G. Meissner, Nucl. Phys. A **747**, 362 (2005).
[63] S. Pastore, S. C. Pieper, R. Schiavilla, and R. B. Wiringa, arXiv:1212.3375 [nucl-th] [Phys. Rev. C (to be published)].
[64] S. C. Pieper, AIP Conf. Proc. **1011**, 143 (2008).
[65] L. E. Marcucci, D. O. Riska, and R. Schiavilla, Phys. Rev. C **58**, 3069 (1998).
[66] L. E. Marcucci, M. Viviani, R. Schiavilla, A. Kievsky, and S. Rosati, Phys. Rev. C **72**, 014001 (2005).
[67] S. Okubo, Prog. Theor. Phys. **12**, 603 (1954).
[68] S. Pastore, R. Schiavilla, and J. L. Goity, Phys. Rev. C **78**, 064002 (2008).
[69] L. Girlanda, S. Pastore, R. Schiavilla, and M. Viviani, Phys. Rev. C **81**, 034005 (2010).
[70] F. Gross, *Relativistic Quantum Mechanics and Field Theory* (Wiley, New York, 1993).